WILEY
Aggregate
Open Access

RESEARCH ARTICLE OPEN ACCESS

Hierarchical Self-Assembled Nanoparticles for Efficient and Eco-Friendly Herbicide Delivery

Yuntian Xiao[1,2,3,4] | Mingyu Chen[4] | Hubiao Jiang[1,2,3] | Hongxun Hao[4] | Qiuxiang Yin[4] | Quan Gao[1,2,3] | Haiqun Cao[1,2,3]

[1]School of Plant Protection, Anhui Agricultural University, Hefei, Anhui Province, People's Republic of China | [2]Anhui Province Engineering Laboratory for Green Pesticide Development and Application, School of Plant Protection, Anhui Agricultural University, Hefei, Anhui Province, People's Republic of China | [3]Anhui Province Key Laboratory of Integrated Pest Management on Crops, School of Plant Protection, Anhui Agricultural University, Hefei, Anhui Province, People's Republic of China | [4]School of Chemical Engineering and Technology, State Key Laboratory of Chemical Engineering, Tianjin University, Tianjin, People's Republic of China

Correspondence: Yuntian Xiao (yuntianxiao@ahau.edu.cn) | Haiqun Cao (caohq@ahau.edu.cn)

Received: 20 November 2025 | **Revised:** 30 January 2026 | **Accepted:** 4 February 2026

Keywords: crop protection | herbicide delivery | hierarchical self-assembly | low leaching | nontarget organism safety

ABSTRACT

Herbicides are indispensable for safeguarding global crop production, yet their effectiveness is often undermined by extensive environmental losses during application. Using herbicide Diuron as a model compound, we developed hierarchical nanoparticles constructed through host–guest molecular recognition followed by electrostatic coassembly, yielding a formulation that unites high delivery efficiency with enhanced environmental compatibility. Relative to conventional wettable powders, these nanoparticles exhibited temperature-responsive release behavior and significantly enhanced foliar adhesion and deposition, increasing leaf retention by more than 241.7%. They also demonstrated strong resistance to rainfall wash-off and a markedly reduced propensity for groundwater leaching, with leaching losses decreased by approximately 18.6%. Greenhouse and field evaluations further confirmed their superior weed control under practical conditions, achieving control efficacies of up to 70.1% against *Abutilon theophrasti* and 52.9% against *Setaria faberi*, compared with 53.7% and 39.1%, respectively, for the commercial formulation at the same application rate. Extensive ecotoxicological assessments encompassing seed germination, zebrafish and earthworm assays, in vitro cellular tests, and in vivo rat studies consistently revealed an improved safety profile compared with commercial and technical formulations. Together, these results highlight hierarchical self-assembled nanoparticles as a promising platform for next-generation herbicide delivery that combines high target utilization with lower environmental impact and greater sustainability.

1 | Introduction

Chemical pesticides remain indispensable to modern agriculture, protecting crops and underpinning food security and economic stability [1–3]. With the global population projected to reach 9.7 billion by 2050 [4], improving productivity is urgent, particularly through effective weed control, since weeds alone cause yield losses of roughly 20%–50% by competing for nutrients, water, and light [5]. Although nearly 2000 herbicidal agents are commercially available [6], their efficacy is frequently compromised by environmental stressors such as heat, wind, and rainfall that drive volatilization, runoff, erosion, and groundwater leaching [7–10]; these processes can form more toxic degradation products and, in some cases, reduce effective utilization to below 1%, amplifying risks to ecosystems and human health [11, 12]. Designing formulations that combine enhanced environmental stability,

This is an open access article under the terms of the Creative Commons Attribution License, which permits use, distribution and reproduction in any medium, provided the original work is properly cited.

© 2026 The Author(s). *Aggregate* published by SCUT, AIEI, and John Wiley & Sons Australia, Ltd.

targeted delivery, and superior ecological safety is therefore critical. Because the discovery of new active ingredients is costly and slow, nanopesticides have attracted increasing attention and were highlighted by IUPAC in 2019 as a transformative chemical innovation [13]. However, most existing systems rely on material-based carriers, and their practical adoption remains limited by unresolved cost–benefit, risk assessment, and field feasibility concerns [14]. Supramolecular self-assembly, driven by hydrophobic effects, electrostatics, π-stacking, charge transfer, and hydrogen bonding, offers a bottom-up, low-cost route to tunable, biocompatible nanopesticides [15–17] that spontaneously form stable, environmentally benign nanostructures with controllable size, morphology, and release kinetics, presenting a promising path toward more efficient and safer herbicide delivery [18].

Host–guest self-assembly offers a molecularly precise route to tailor pesticide behavior by harnessing hydrogen bonding, hydrophobic effects, and conformational adaptation [19, 20]. Macrocyclic hosts, such as cyclodextrins, crown ethers, calix[n]arenes, cucurbit[n]urils, and pillar[n]arenes, could substantially improve solubility, stability, and wettability, enabling safer, more targeted delivery [21–24]. For example, cucurbit[8]uril-paraquat-azobenzene supramolecular vesicles afford UV-triggered release with reduced toxicity [25], while β-cyclodextrin complexes (with azobenzene or ferrocene derivatives) enable light-controlled release and enhanced foliar affinity and antibiofilm activity [26, 27]. To date, most efforts modify host or guest individually or rely on ternary assemblies; a pressing challenge is whether higher order, multidimensional architectures founded on host–guest inclusion can be rationally constructed to consolidate stability, stimulus responsiveness, and biological efficacy.

Hierarchical molecular self-assembly in solution enables preprogrammed construction of complex architectures with dynamic properties [28, 29]. Typically, primary building blocks first organize into lower order motifs that integrate into higher order structures [30]. Zhang et al. [31] reported that a coassembled system of sulfobutyl ether-β-cyclodextrin (SBE-β-CD) with tebuconazole and poly(dimethyldiallylammonium chloride) achieved controlled fungicide release and markedly enhanced antifungal efficacy. He et al. further designed a nanodelivery platform combining a β-CD-NH_2-tebuconazole inclusion complex with prothioconazole loaded into mPEG-b-PLG derived from poly-γ-glutamic acid, which enabled pH-responsive release, uniform deposition, synergistic suppression of *Fusarium graminearum*, and favorable plant safety [32]. However, such hierarchical supramolecular strategies have rarely been extended to herbicide delivery, particularly in the context of complex, field-relevant application scenarios, which remain largely unexplored. Inspired by these advances, we introduce a dual-stage hierarchical self-assembly strategy that integrates host–guest recognition and electrostatic interactions to construct efficient and biocompatible nanoparticles. As a model system, Diuron, a widely used systemic herbicide applied globally for weed control, was selected; it exerts its herbicidal activity primarily through inhibition of photosystem II. SBE-β-CD first forms an inclusion complex with Diuron, which subsequently coassembles with positively charged chitosan to yield nanoparticles exhibiting high water stability, uniform dispersion, and tunable particle size. As shown in Figure 1, this work advances existing delivery systems by introducing a dual-stage hierarchical architecture, demonstrating enhanced field-relevant performance, and providing multitier ecotoxicity validation, thereby clarifying the practical relevance and biosafety of the proposed system.

As shown in Figure 1, this design achieves simultaneous enhancement of eight key attributes encompassing pH- and temperature-responsive release, photostability, foliar wettability and rainfastness, systemic absorption and translocation, herbicidal efficacy, reduced soil leaching, improved environmental biosafety, and minimized toxicity to human cells and rat models.

2 | Results and Discussion

2.1 | Molecular Recognition, Host–Guest Self-Assembly, and Electrostatic Self-Assembly

The preparation of the nanoparticles is based on molecular recognition and host–guest self-assembly between Diuron and SBE-β-CD, as illustrated in Figure 2a. The formation of this inclusion complex is driven primarily by the displacement of water molecules from the hydrophobic cavity of SBE-β-CD, accompanied by establishment of van der Waals interactions, hydrophobic effects, and hydrogen bonding between the guest and host molecules [33, 34].

Complexation depends on both spatial fit and thermodynamic stability [35]. When Diuron, which has limited aqueous solubility of approximately 0.448 mg/L at 25°C, is vigorously shaken and sonicated in water it yields a turbid suspension that becomes transparent upon stepwise addition of SBE-β-CD, consistent with guest encapsulation and enhanced apparent solubility (Figure 2b). ^{1}H NMR of a filtered 1:1 Diuron:SBE-β-CD solution in D_2O resolves Diuron resonances at 7.34, 7.43, 7.84, and 2.90 ppm assigned to H1′, H2′, H3′ and H5′, together with shifts of the cyclodextrin internal protons H3 (+0.002 ppm) and H5 (−0.014 ppm; Figure 2c). The shielding effect observed for the proton H5, situated at the wider rim of the SBE-β-CD cavity, shows increased electron density and implies preferential entry of the Diuron molecules through this wider end of the truncated conical cavity. 2D NOESY spectra further confirmed clear cross-peaks between SBE-β-CD H3 and Diuron H1′, H2′, and H3′, confirming insertion of the aromatic end into the cavity and a benzene-ring-first orientation (Figure 2d).

Additionally, the inclusion stoichiometry of the Diuron/SBE-β-CD complex was investigated using the Benesi–Hildebrand equation and phase solubility diagrams. UV absorption spectroscopy revealed a progressive decrease in Diuron's characteristic absorbance at 248.5 nm with increasing SBE-β-CD concentration (Figure 2e), in evidence of electronic perturbations induced by inclusion interactions or displacement of water molecules [36]. The Benesi–Hildebrand method was further employed to quantitatively analyze the stoichiometry and to determine the binding constant (K) of the Diuron/SBE-β-CD inclusion complex by monitoring absorbance changes of Diuron at varying SBE-β-CD concentrations [37]. A plot of the reciprocal absorbance difference ($1/\Delta A$) against the reciprocal concentration of SBE-β-CD exhibited a strong linear correlation ($R^2 = 0.9981$, Figure 2f,g), unequivocally confirming a 1:1 host–guest stoichiometry, with

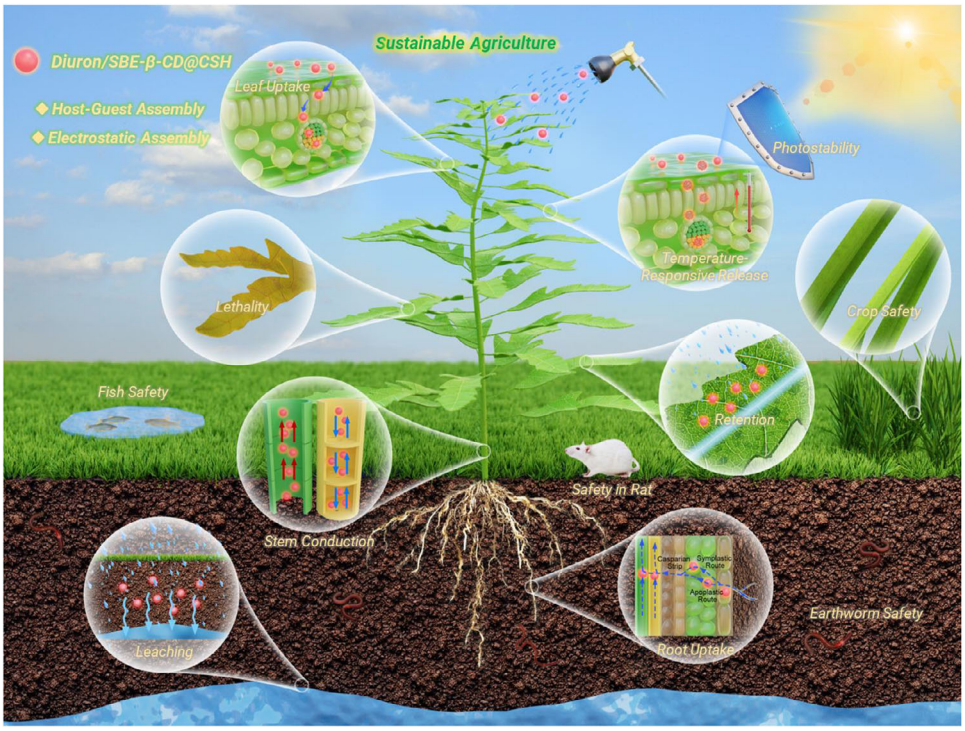


FIGURE 1 | Conceptual framework of herbicide nanoparticle effectiveness and sustainability. The schematic shows hierarchical host–guest and electrostatic self-assembly of Diuron/SBE-β-CD@CSH that enables enhanced herbicide efficacy and reduced toxicity.

binding constant $K = 675.49\ M^{-1}$. The phase solubility diagram displayed linear enhancement in Diuron solubility with increasing SBE-β-CD concentrations (Figure 2h), in support of the stable 1:1 inclusion complex [38].

The Diuron/SBE-β-CD inclusion complex prepared by slow solvent evaporation was characterized by powder X-ray diffraction (PXRD), Fourier-transform infrared (FTIR) spectroscopy, and differential scanning calorimetry (DSC). Pure Diuron exhibited sharp diffraction peaks at 11.7°, 13.3°, 15.3°, 17.1°, 20.8°, 21.8°, and 24.9°, consistent with a crystalline phase (Figure 2i), whereas SBE-β-CD showed a broad amorphous halo. The complex's PXRD closely matched the amorphous profile of SBE-β-CD and lacked Diuron reflections, indicating encapsulation-induced amorphization. FTIR spectra corroborated complex formation (Figure 2j): SBE-β-CD bands at 3372 cm^{-1} (O–H), 1649 cm^{-1} (C═O), 1153 cm^{-1} (C–O–C), and 1026 cm^{-1} (S═O) experienced red shifts, Diuron absorptions in the 400–1600 cm^{-1} region were largely obscured, and the N–H and C═O bands shifted from 3278 cm^{-1} and 1469 cm^{-1} to 3384 cm^{-1} and 1652 cm^{-1}, respectively, consistent with strengthened hydrogen bonding. DSC analysis showed the disappearance of the melting endotherm of Diuron at 159.91°C and a shift in the decomposition-related peak of SBE-β-CD from 264.2°C to 275.6°C in the formulation (Figure 2k), indicating an alteration in the solid-state thermal behavior.

Following the formation of the host–guest inclusion complex, chitosan, a biodegradable, and biocompatible natural polymer, was introduced to facilitate electrostatic self-assembly with Diuron/SBE-β-CD (Figure 3a). The effect of varying mass ratios (ranging from 1:1 to 1:2) on nanoparticle formation was studied (Figure 3b). The results revealed a characteristic U-shaped trend, where particle size and polydispersity index (PDI) initially decreased before increasing. As the CSH/SBE-β-CD mass ratio decreased, the appearance of the nanoparticle suspensions transitioned from clear to opalescent, ultimately resulting in visible aggregation, accompanied by a reduction in ζ-potential (Figure 3c). At the lowest mass ratio tested (1:2), severe aggregation occurred, leading to rapid particle precipitation within 30 min and a minimal ζ-potential of 10.8 mV.

At a CSH/SBE-β-CD mass ratio of 1:1, limited intermolecular and intramolecular cross-linking between chitosan and SBE-β-CD resulted in sparse formation of heterogeneous nanoparticles, leaving a substantial amount of free chitosan in solution. Consequently, both particle size and PDI values increased [39, 40]. Gradual reduction of the mass ratio from 1:1 to 1:1.8 enhanced the cross-linking efficiency, steadily reducing both particle size and PDI. However, at mass ratios below 1:1.9, excessive cross-linking triggered particle agglomeration, with substantial increase in particle size and PDI [40]. The mass ratio of 1:1.8 was found to be optimal, yielding nanoparticles with an average diameter of 172.63 nm (Figure 3e), notably low PDI of 0.09177, and stable ζ-potential of 25.2 mV. HPLC quantification (Figure S1) further revealed loading capacity (LC) of 10.3871% and an encapsulation efficiency (EE) of 57.4386%. In the SEM and TEM images (Figure 3f,g), the Diuron/SBE-β-CD@CSH nanoparticles were observed to have relatively uniform spherical morphology, and selected-area electron diffraction (SAED) patterns verified they were amorphous. Colloidal stability tests performed over 12 days demonstrated sustained particle size and ζ-potential during the initial 4 days (Figure 3d). Mild aggregation and sedimentation were observed after 12 days, indicating slight loss of stability over extended storage [41–43].

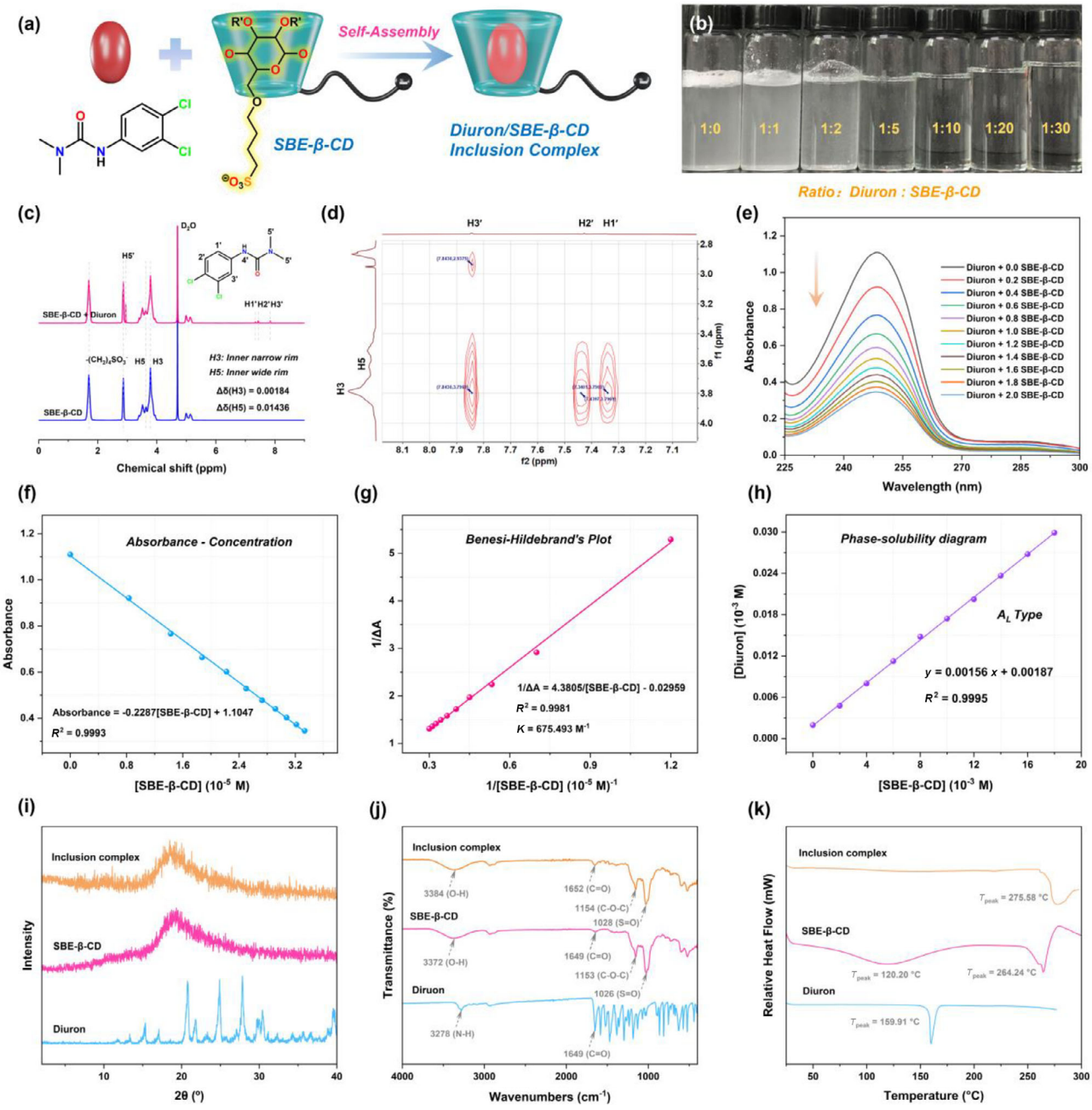


FIGURE 2 | Preparation and characterization of the inclusion complex. (a) Schematic diagram illustrating the formation of the Diuron/SBE-β-CD binary inclusion complex. (b) Turbidity changes of aqueous Diuron suspensions upon incremental addition of SBE-β-CD. (c) ^{1}H NMR (D_2O) of pure SBE-β-CD (bottom) and an aqueous mixture of SBE-β-CD with equimolar Diuron added (top, filtered). (d) ^{1}H-^{1}H 2D NOESY spectrum (D_2O) of an aqueous mixture containing equimolar amounts of SBE-β-CD and Diuron (filtered). (e) UV absorption spectra of Diuron solutions with varying mole fractions of SBE-β-CD. (f) Benesi–Hildebrand plot ($1/\Delta A$ vs. 1/[SBE-β-CD]) derived from UV absorption data. (g) Linear correlation between the Diuron absorbance at 248.5 nm and mole fraction of SBE-β-CD. (h) Phase solubility diagram of Diuron as a function of SBE-β-CD concentration. (i–k) Powder X-ray diffraction patterns (i), Fourier-transform infrared spectra (j), and differential scanning calorimetry curves (k) of Diuron, SBE-β-CD, and the Diuron/SBE-β-CD inclusion complex.

2.2 | Stimuli-Responsive Release and Photostability

Chenopodium serotinum L. is a highly invasive dicot common in temperate and subtropical croplands [44]. Its prolific seed production, germination across temperatures from 15°C to 40°C and tolerance of soil pH from 4.5 to 8.3 underpin its competitive dominance and drive substantial yield losses worldwide [45, 46]. Stimuli-responsive nanosystems offer an adaptable strategy for herbicide delivery by triggering release in response to temperature or pH cues, thereby synchronizing dosing with peak weed growth and accommodating soil heterogeneity to enhance efficacy while minimizing off target losses [47].

Within this context, we investigated the impact of temperature and pH on the release profile of the Diuron/SBE-β-CD@CSH

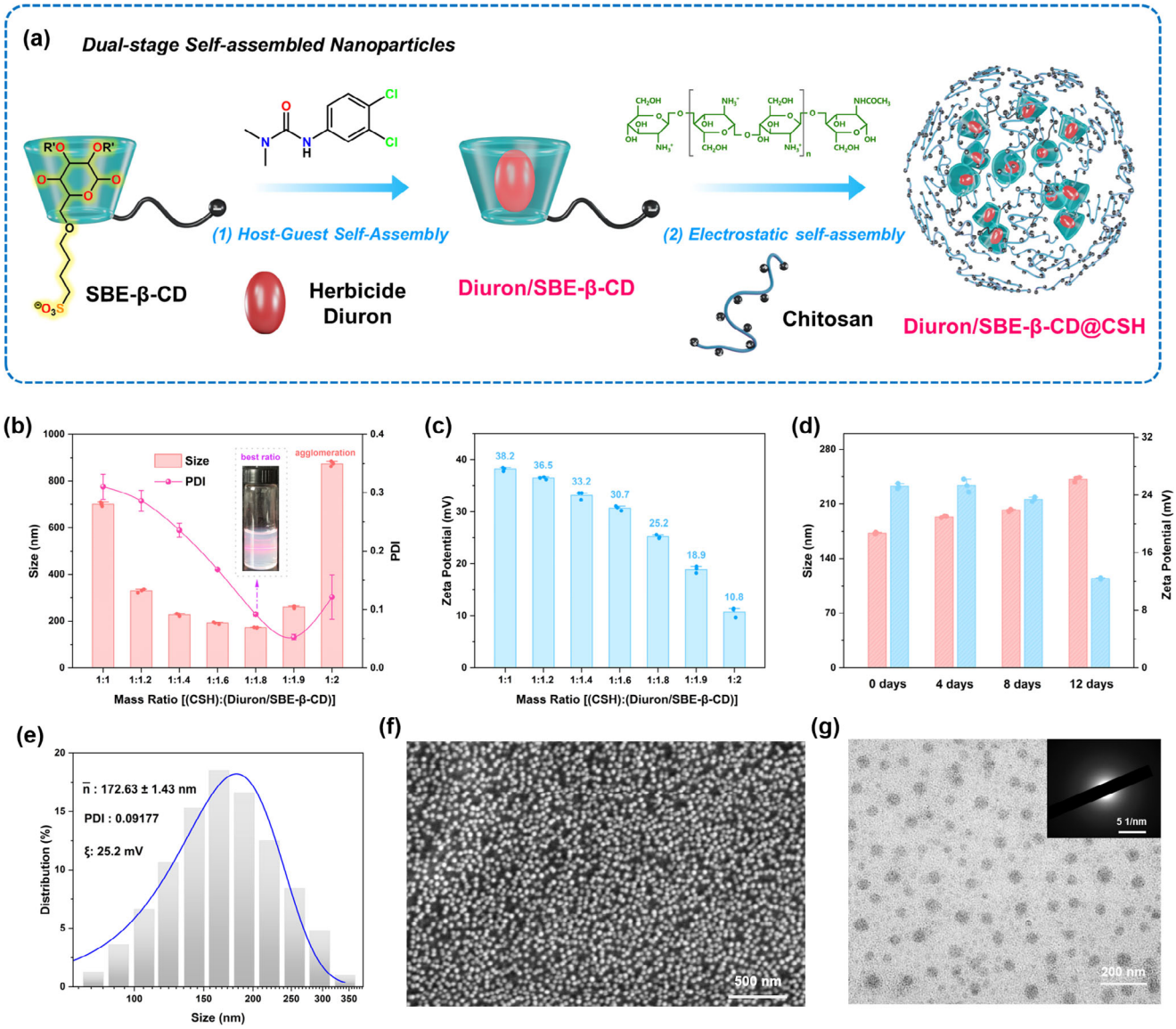


FIGURE 3 | Assembly and characterization of the herbicide nanoparticles. (a) Schematic illustration of the hierarchical self-assembly of Diuron/SBE-β-CD@CSH nanoparticles via host–guest inclusion and electrostatic interactions. (b) Particle size and polydispersity index (PDI) of Diuron/SBE-β-CD@CSH nanoparticles prepared at different Diuron/SBE-β-CD-to-CSH mass ratios (independent experiments: $n = 3$; the data are presented as mean ± standard deviation). (c) ς-potential of Diuron/SBE-β-CD@CSH nanoparticles at varying mass ratios (independent experiments: $n = 3$; the data are presented as mean ± standard deviation). (d) Stability evaluation of particle size and ς-potential for Diuron/SBE-β-CD@CSH nanoparticles (mass ratio of 1.8:1) over 16 days at 25°C (independent experiments: $n = 3$; the data are presented as mean ± standard deviation). (e–g) Particle size distribution (e), SEM (f), TEM images, and corresponding SAED pattern (g) of Diuron/SBE-β-CD@CSH nanoparticles (mass ratio of 1.8:1).

nanodelivery system. As shown in Figure 4a, Diuron release exhibited a clear temperature dependence. After 72 h, cumulative release at 35°C reached 90.86%, significantly higher than at 25°C (82.48%) and 15°C (77.49%). Intrinsic dissolution rates (IDRs) were calculated for the first 7 h, with values of 0.16733 mg/h at 15°C, 0.37108 mg/h at 25°C, and 0.72876 mg/h at 35°C (Figure 4c), demonstrating enhanced release at higher temperatures. This temperature-triggered release behavior is attributed to increased molecular dynamics at elevated temperatures, which reduce noncovalent interactions, such as van der Waals forces, and promote Diuron diffusion from the nanoparticle matrix [48]. The stability of the Diuron/SBE-β-CD complex is temperature-dependent; higher temperatures weaken stabilizing hydrogen bonds and hydrophobic interactions, facilitating Diuron release from the SBE-β-CD cavity [49, 50].

pH responsiveness is another crucial factor in the release kinetics of Diuron from Diuron/SBE-β-CD@CSH. Release profiles at pH 4.5, 6.8, and 8.4 at 25°C (Figure 4b) revealed enhanced release under acidic conditions, with cumulative Diuron release reaching 91.96% at pH 4.5 after 72 h, compared to 82.67% at pH 6.8 and 87.57% at pH 8.4. IDR analysis (Figure 4d) showed the lowest release rate at pH 6.8 (0.24383 mg/h), while rates at pH 4.5 (0.29342 mg/h) and pH 8.4 (0.29122 mg/h) were similar. In acidic conditions, protonation of chitosan amino groups ($-NH_2$) to positively charged $-NH_3^+$ increases polymer solubility and

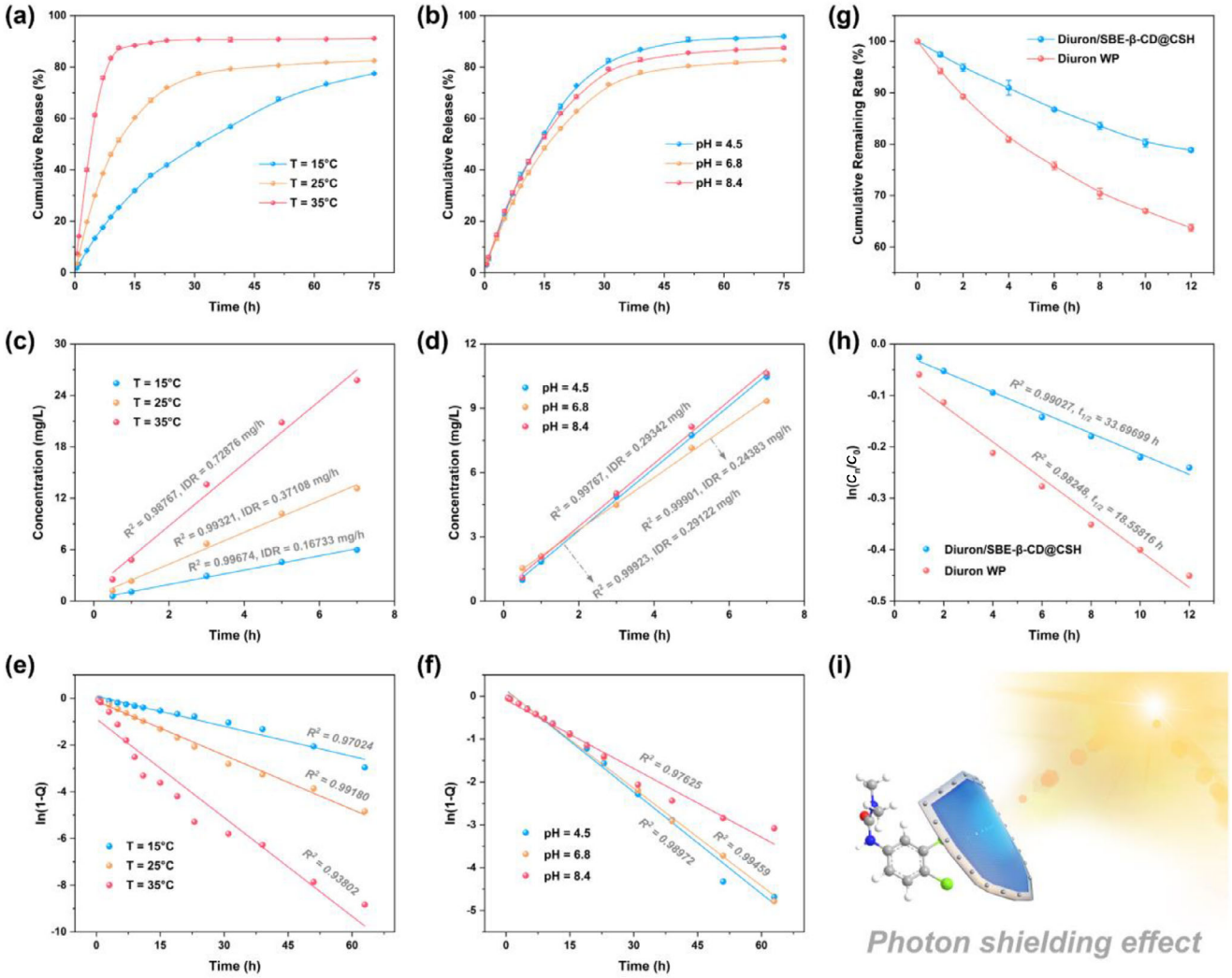


FIGURE 4 | Release behaviors and photolysis behaviors of the herbicide. (a, b) Release profiles of Diuron/SBE-β-CD@CSH nanoparticles at different temperatures (a; 15°C, 25°C, 35°C) and pH conditions (b; 4.5, 6.8, 8.4). Independent experiments: $n = 3$; the data are presented as mean ± standard deviation. (c, d) Intrinsic dissolution rate (IDR) curves of Diuron/SBE-β-CD@CSH at varying temperatures (c) and pH levels (d). Independent experiments: $n = 3$; the data are presented as mean ± standard deviation. (e, f) First-order kinetic fitting curves for Diuron/SBE-β-CD@CSH release under different temperatures (e) and pH conditions (f). (g) Cumulative residual percentages of active components in Diuron WP and Diuron/SBE-β-CD@CSH under UV irradiation over time. Independent experiments: $n = 3$; the data are presented as mean ± standard deviation. (h) Pseudo-first-order kinetic degradation curves of Diuron WP and Diuron/SBE-β-CD@CSH nanoparticles under UV irradiation. (i) Schematic illustration showing enhanced photostability of Diuron encapsulated within Diuron/SBE-β-CD@CSH nanoparticles.

causes electrostatic repulsion between polymer chains, facilitating Diuron diffusion [51]. Under alkaline conditions (pH 8.4), deprotonation of chitosan weakens the electrostatic interactions and leads to a more relaxed, porous matrix, promoting Diuron release, though less efficiently than in acidic conditions [52]. Kinetic modeling (Table S3 and Figure 4e,f) showed that the first-order model ($R^2 > 0.93$) provided the best fit to the release data, indicating a concentration-dependent release behavior with progressively decreasing release rates. Meanwhile, analysis using the Ritger–Peppas model yielded release exponent values (n) in the range of 0.45–0.85 (Table S3), which is characteristic of anomalous (non-Fickian) transport, suggesting that Diuron release is jointly governed by diffusion through the swollen chitosan matrix and matrix dissolution/relaxation rather than by a single rate-limiting mechanism [53].

The photostability of Diuron is also crucial for its long-term effectiveness in weed control, particularly under intense summer sunlight [54]. To assess this, the photostability of Diuron/SBE-β-CD@CSH was evaluated under simulated UV radiation for 12 h. As shown in Figure 4g, Diuron/SBE-β-CD@CSH exhibited significantly enhanced photostability, retaining 80.00% of its active ingredient compared to 68.70% for commercial Diuron WP. Both formulations followed pseudo-first-order photodegradation kinetics (Table S4, $R^2 > 0.98$), with rate constants of 0.02003 h^{-1} for Diuron/SBE-β-CD@CSH and 0.03538 h^{-1} for Diuron WP. The photodegradation half-life of Diuron/SBE-β-CD@CSH increased to 33.70 h, an 81.58% improvement over Diuron WP's half-life of 18.56 h (Figure 4h). This enhanced photostability is attributed to two protective mechanisms: the encapsulation of Diuron within the SBE-β-CD cavity, which shields it from UV

degradation, and the chitosan component, which absorbs and scatters UV radiation. These results highlight that Diuron/SBE-β-CD@CSH nanoparticles significantly improve Diuron's photostability (Figure 4i), thereby enhancing field utilization, reducing costs, and minimizing environmental impact.

2.3 | Interfacial Performance on Weed Leaves

Optimized wettability and rainfastness enhance uniform spreading and uptake on leaf surfaces, reduce wash-off, and therefore lower reapplication frequency and offsite runoff [55, 56]. We then compared Diuron/SBE-β-CD@CSH with pure water and a commercial Diuron wettable powder. Viscosity and density were comparable across formulations (Figures 5a and S2), but surface activity differed substantially. Surface tension declined from 71.903 mN/m for water to 68.156 mN/m for the commercial formulation and to 62.103 mN/m for Diuron/SBE-β-CD@CSH, consistent with enhanced wettability driven by chitosan surface activity [57, 58]. Dynamic contact angle measurements on *Chenopodium serotinum* L. leaves confirmed improved spreading, with steady angles of 118.30° for water, 114.15° for the wettable powder and 102.75° for Diuron/SBE-β-CD@CSH (Figure 5b and Supporting Information Video 1). Leaf liquid-holding capacity increased from 0.9316 mg/cm^2 for water and 1.3593 mg/cm^2 for the wettable powder to 4.6461 mg/cm^2 for Diuron/SBE-β-CD@CSH (Figure 5c), demonstrating markedly greater adhesion. This enhancement likely arises from robust hydrogen-bond interactions between functional groups (–OH, $-NH_2$, $-SO_3^-$) present on nanoparticle surfaces and epicuticular wax components such as fatty acids, alcohols, and aldehydes, thereby facilitating superior retention, thereby circumventing the addition of surfactants [59].

In foliar herbicide applications, understanding droplet impact dynamics on hydrophobic weed surfaces is essential for optimizing spray deposition and droplet retention. Using computational fluid dynamics (CFD) simulations with a volume of fluid (VOF) continuous-phase model [60, 61], we examined the droplet impact behavior of Diuron WP and Diuron/SBE-β-CD@CSH formulations. Simulations of droplets falling from an 8.0 mm height over 30 ms revealed four distinct phases: initial contact, spreading, retraction, and rebound (Figure 5d and Supporting Information Video 2). Detailed velocity field analyses (Figures S4–S6) offered valuable insights into the fluid dynamics of each phase.

Upon initial impact (0 ms), droplets of pure water exhibited high velocity concentration at their leading edges, dominated by vertical velocity (v) due to gravitational acceleration. Within 10 ms, droplets spread laterally, forming symmetrical horizontal (u) velocity lobes. Between 10–20 ms, retraction occurred, characterized by inward velocity vectors, central jets, and peripheral vortices, indicative of complex fluid–air interfacial interactions. By 25 ms, droplets elongated vertically, initiating rebound as lateral kinetic energy transitioned into vertical ascent, manifested as pronounced upward velocities at 30 ms. Diuron WP droplets also largely mirrored this behavior, although with a slight delay in rebound initiation and reduced rebound height (Figure S5). In marked contrast, Diuron/SBE-β-CD@CSH droplets demonstrated delayed retraction and remained adhered throughout the entire 30 ms period, attributable to more efficient dissipation and redistribution of horizontal kinetic energy (Figure S6). These dynamics were quantified by normalized rebound height (H_t/D_0). The value for Diuron/SBE-β-CD@CSH (0.5999) was notably lower compared to that of pure water (0.6269) and commercial Diuron WP (0.6267). Experimental validation conducted on *Chenopodium serotinum* L. leaves corroborated CFD simulation outcomes (Figure 5e and Supporting Information Video 3). Normalized rebound heights were highest for pure water droplets (1.0233), intermediate for Diuron WP (0.6206), and lowest for Diuron/SBE-β-CD@CSH (0.5681; Figure 5f). Minor discrepancies observed between simulation and experiments likely resulted from inherent variability in leaf surface characteristics, such as microscale roughness and slight inclination angles. Nevertheless, the current simulations did not account for factors such as leaf surface roughness and waxy microstructures; incorporating these features into future CFD modeling is expected to further improve the accuracy of the simulations.

Rainfastness is another decisive factor for herbicide persistence and field performance [62]. SEM imaging showed that commercial Diuron WP deposited as irregular, aggregated clumps on the highly textured surface of *Chenopodium serotinum* L. leaves, most of which were dislodged by simulated rainfall (Figures S7 and S8b). In contrast, Diuron/SBE-β-CD@CSH formed a uniform nanoparticulate layer that lodged within leaf microcrevices and persisted after washing (Figure S8d). Confocal laser scanning microscopy (CLSM) of FITC-labeled formulations corroborated these morphologies: both treatments produced strong fluorescence before wash, but after wash the self-assembled nanoparticles retained robust fluorescence across the lamina while the signal from Diuron WP was largely lost and confined to residual aggregates along primary veins (Figure 5g). HPLC quantification confirmed substantially greater leaf retention for Diuron/SBE-β-CD@CSH, 47.90% versus 27.96% for Diuron WP (Figure 5h), a result that supports enhanced rainfastness, prolonged foliar exposure, and reduced off target losses in the field.

2.4 | Uptake, Conduction, and Lethality

Absorption and systemic translocation within target weeds govern herbicidal efficacy for both foliar and root applications [63]. Diuron, a substituted urea herbicide with both contact and systemic activity, is taken up through leaves and roots [64]. Formulated as Diuron/SBE-β-CD@CSH nanoparticles with a mean diameter of 172.63 nm, this system exploits nanoscale size and the plant-compatible properties of SBE-β-cyclodextrin and chitosan to enhance uptake and systemic distribution, thereby improving overall herbicidal performance. CLSM conducted 24 h post-treatment demonstrated effective long-distance translocation of Diuron/SBE-β-CD@CSH nanoparticles within *Chenopodium serotinum* L., following both root and foliar applications (Figure 6a). After root treatment, intense green fluorescence was clearly visible at the root surface, especially within root hairs and epidermal cells, confirming efficient initial uptake. Fluorescent signals indicated that nanoparticles were present within the root cortex and were subsequently detected in the central stele. Signals observed in pericycle cells suggested nanoparticle entry into the vascular region. In addition, fluorescence detected in vascular bundles of stems and leaf veins demonstrated long-distance translocation from roots to aerial tissues [65, 66]. Within leaf tissues, nanoparticles prominently

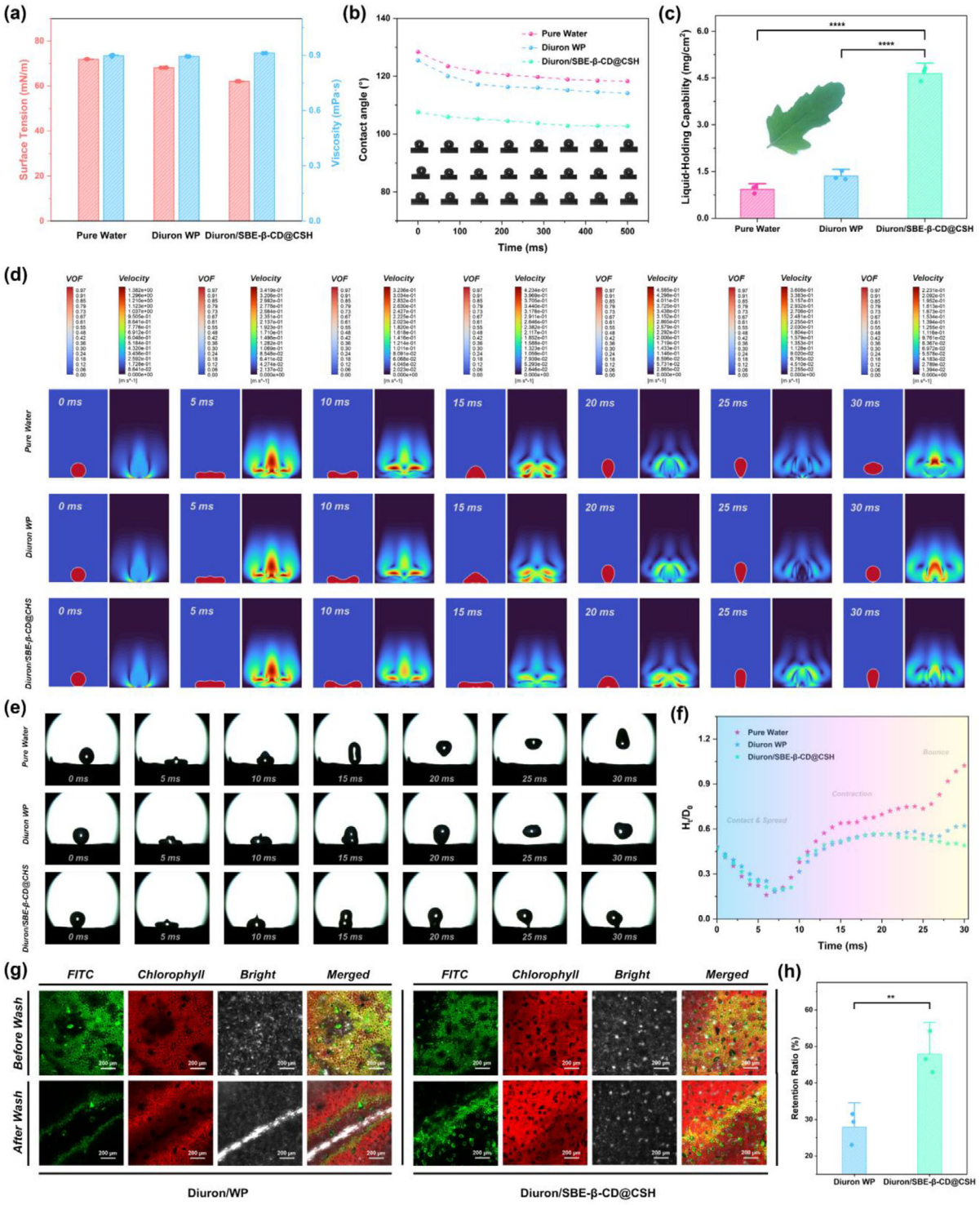


FIGURE 5 | Surface adhesion and retention of the nanoparticle formulation. (a) Dynamic surface tension of pure water, Diuron WP, and Diuron/SBE-*β*-CD@CSH solutions at 100 mg/L active ingredient concentration. Independent experiments: $n = 3$; the data are presented as mean ± standard deviation. (b) Dynamic contact angle images of droplets for pure water, Diuron WP, and Diuron/SBE-*β*-CD@CSH solutions on *Chenopodium serotinum* L. leaves. Independent experiments: $n = 3$; the data are presented as mean ± standard deviation. (c) Liquid-holding capacity of *Chenopodium serotinum* L. leaves treated with pure water, Diuron WP, and Diuron/SBE-*β*-CD@CSH solutions. Independent measurements: $n = 3$; the data are presented as mean ± standard deviation. (d) CFD simulation maps showing volume fraction and velocity distributions for droplets of pure water, Diuron WP, and Diuron/SBE-*β*-CD@CSH impacting a hydrophobic surface. (e) Sequential images of droplet impact behavior for pure water, Diuron WP, and Diuron/SBE-*β*-CD@CSH solutions on *Chenopodium serotinum* L. leaves. (f) Normalized droplet rebound height (H_t/D_0) versus time for pure water, Diuron WP, and Diuron/SBE-*β*-CD@CSH solutions on *Chenopodium serotinum* L. leaves. (g) Confocal microscopy images of *Chenopodium serotinum* L. leaf surfaces treated with Diuron WP and Diuron/SBE-*β*-CD@CSH, before and after simulated rainfall. (h) Retention of active ingredients on leaf surfaces after rain-wash tests for Diuron WP and Diuron/SBE-*β*-CD@CSH. Independent measurements: $n = 3$; the data are presented as mean ± standard deviation.

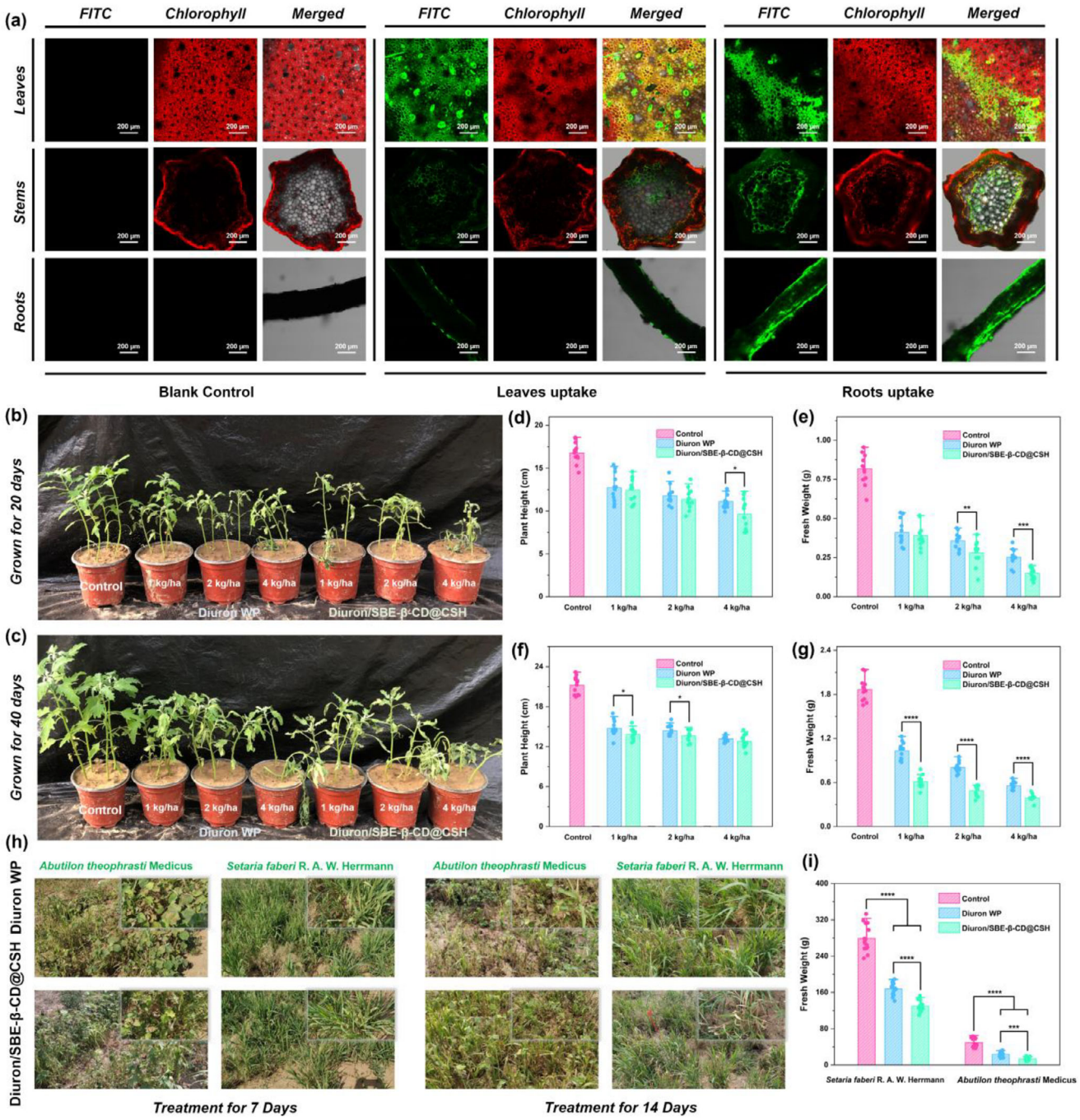


FIGURE 6 | Uptake, conduction, and lethality of the nanoparticle formulation. (a) Confocal images of *Chenopodium serotinum* L. treated with FITC-loaded Diuron/SBE-*β*-CD@CSH nanoparticles, illustrating nanoparticle distribution (green fluorescence) in roots, stems, and leaves, along with chloroplast autofluorescence (red). (b–e) Visual assessments (b), plant heights (d), and fresh weights (e) of *Chenopodium serotinum* L. grown for 20 days, followed by 20-day treatments with pure water, Diuron WP, and Diuron/SBE-*β*-CD@CSH at various doses. Number of measurements: $n = 12$, across three independent experiments. (c–g) Visual assessments (c), plant heights (f), and fresh weights (g) of *Chenopodium serotinum* L. grown for 40 days, followed by similar 20-day treatments. Number of measurements: $n = 12$ across three independent experiments; the data are presented as mean ± standard deviation. (h, i) Field photographs (h) and fresh weight comparisons (i) of *Abutilon theophrasti* Medicus (5–6 leaf stage) and *Setaria faberi* R. A. W. Herrmann (20–30 cm height) 21 days after treatment with Diuron WP and Diuron/SBE-*β*-CD@CSH. Number of measurements: $n = 10$, across three independent experiments; the data are presented as mean ± standard deviation.

accumulated in mesophyll cells, showing clear colocalization of green fluorescence (nanoparticles) with red chlorophyll fluorescence, suggesting direct interactions with chloroplasts. Following foliar application, even stronger nanoparticle fluorescence signals closely overlapped intrinsic red chlorophyll fluorescence, indicative of highly efficient intracellular targeting. Leaf entry likely occurred via stomatal openings (5–10 μm diameter, Figure S7) or through direct cuticular penetration [67, 68]. Furthermore, robust green fluorescence signals observed within stem vascular bundles demonstrated efficient downward phloem-mediated

translocation toward the roots [69]. Terminal fluorescence in root cross-sections confirmed basipetal movement into root zones, though nanoparticles localized here posed minimal risk of interfering with photosynthetic processes.

The self-assembled nanoparticle formulation Diuron/SBE-β-CD@CSH significantly enhances interfacial wettability, retention, molecular stability, uptake, and systemic translocation of Diuron, collectively suggesting improved herbicidal efficacy. Its performance was evaluated against *Chenopodium serotinum* L. under greenhouse conditions at two distinct growth stages (20 and 40 days). Compared to untreated controls, Diuron WP exhibited clear dose-dependent phytotoxic symptoms, including leaf chlorosis and stem wilting (Figure 6b,c), with the most severe effects observed at the highest application rate (4 kg/ha). At equivalent dosages, Diuron/SBE-β-CD@CSH consistently exhibited stronger inhibitory effects. Key physiological parameters such as plant height and fresh weight were assessed across treatments. At the 20-day stage and a dosage of 4 kg/ha, Diuron WP reduced plant height and fresh weight by 33.81% and 69.10%, respectively, whereas Diuron/SBE-β-CD@CSH exerted more substantial suppression, reducing height by 36.81% and fresh weight by 77.60% at the same dosage (Figure 6d,e). By the 40-day stage, the nanoparticle formulation continued to demonstrate superior efficacy, achieving at least an 8.82% greater reduction in fresh weight compared to Diuron WP (Figure 6g), with a statistically significant advantage of 22.53% observed at the 1 kg/ha dose ($p < 0.05$). Although these relative benefits decreased at higher doses during later growth stages, likely due to structural maturation and activation of adaptive resistance mechanisms [70], Diuron/SBE-β-CD@CSH consistently provided superior weed suppression even at lower application rates.

To validate the efficacy of Diuron/SBE-β-CD@CSH nanoparticles beyond controlled greenhouse conditions, field trials were conducted in three cornfields (~20 m^2 each) predominantly infested with *Abutilon theophrasti* Medicus (5–6 leaf stage) and *Setaria faberi* R. A. W. Herrmann (20–30 cm height). At an application dosage of 1500 g/ha, visible phytotoxic symptoms emerged within 7 days and progressively intensified by Day 14, characterized by leaf desiccation, curling, chlorosis, and lodging, particularly pronounced in *Abutilon theophrasti* due to its broader leaf morphology (Figure 6h). By Day 21, the nanoparticle formulation demonstrated significantly improved weed control compared to the commercial Diuron WP (Figure S9), achieving control efficacies of 70.09% against *Abutilon theophrasti* and 52.93% against the relatively more mature *Setaria faberi*, in contrast to 53.72% and 39.09%, respectively, for Diuron WP. Additionally, robust herbicidal efficacy was observed against some mature *Chenopodium album* L. plants (50–60 cm), with Diuron/SBE-β-CD@CSH inducing severe chlorosis, stem curling, and lodging, markedly exceeding effects observed with the commercial formulation (Figure S10).

Collectively, these field observations corroborate the greenhouse findings, indicating that the nanoparticle-based formulation can deliver enhanced weed control under practical field conditions at equivalent application rates. Nevertheless, a comprehensive evaluation of the comparative advantages of this nanoformulation will require further multisite field trials conducted according to pesticide label directions for specific cropping systems, over extended timeframes. In particular, future studies should assess key aspects of environmental behavior, such as leaching and runoff potential, as recent meta-analyses have highlighted that the field performance and environmental fate of nanopesticides may differ substantially from laboratory or greenhouse predictions. Despite these considerations, the present results provide a strong foundation supporting the potential of self-assembled nanoparticle-based herbicide formulations for further field-oriented development and risk–benefit evaluation.

2.5 | Leaching Performance and Environmental Impact

For sustainable agriculture, understanding the environmental fate of pesticides and their impacts on nontarget ecosystems is of paramount importance [71, 72]. Rainfall and irrigation during field applications often accelerate pesticide leaching and runoff, posing risks to groundwater and aquatic environments [73]. To evaluate these processes, soil column experiments (Figure 7a) were conducted to compare the migration of Diuron in conventional WP and self-assembled Diuron/SBE-β-CD@CSH formulations under simulated rainfall. Breakthrough and cumulative leaching profiles over 13 days (Figure 7b,c) revealed markedly enhanced soil retention with Diuron/SBE-β-CD@CSH. Maximum leaching occurred later and at a lower level (6.36% on Day 7) compared with Diuron WP (9.18% at an earlier stage), and cumulative leaching by Day 13 was reduced by 18.61%. Residual analysis further confirmed this improvement, with 38.24% of applied Diuron retained in the Diuron/SBE-β-CD@CSH group versus 22.09% in the Diuron WP treatment (Figure S11). The superior retention is attributed to the nanoscale architecture of the self-assembled particles, which provides extensive surface area for interaction with soil components [74, 75], together with the positively charged chitosan shell that enhances electrostatic binding to negatively charged soil particles and organic matter [76]. These synergistic effects effectively reduce herbicide mobility and leaching potential, thereby facilitating more efficient root-mediated uptake of the nanoparticles by weeds within the soil, in agreement with the aforementioned absorption and translocation behaviors, and collectively underscoring the environmental application potential of this supramolecular nanoformulation.

Environmental safety for nontarget organisms is a critical consideration, particularly for pre-emergent herbicides such as Diuron. To evaluate potential ecological toxicity, the effects of Diuron TC, Diuron WP, and Diuron/SBE-β-CD@CSH were assessed in representative nontarget species, including crop seeds (cucumber and rice), aquatic organisms (zebrafish), and soil invertebrates (earthworms). Seed germination assays conducted across eight herbicide concentrations (1.25–160 mg/L) revealed that at lower concentrations (1.25–20 mg/L), all formulations maintained 100% germination rates for both cucumber and rice seeds, indicating negligible acute germination toxicity at these levels (Figures S12 and S13). However, significant differences in total seed and seedling biomass emerged among treatments. Specifically, at 20 mg/L, Diuron/SBE-β-CD@CSH enhanced total biomass by 27.40% and 13.35% in cucumber and rice seeds, respectively, compared to Diuron TC, and by 17.88% and 5.74%, respectively, compared to Diuron WP (Figure 7d–f).

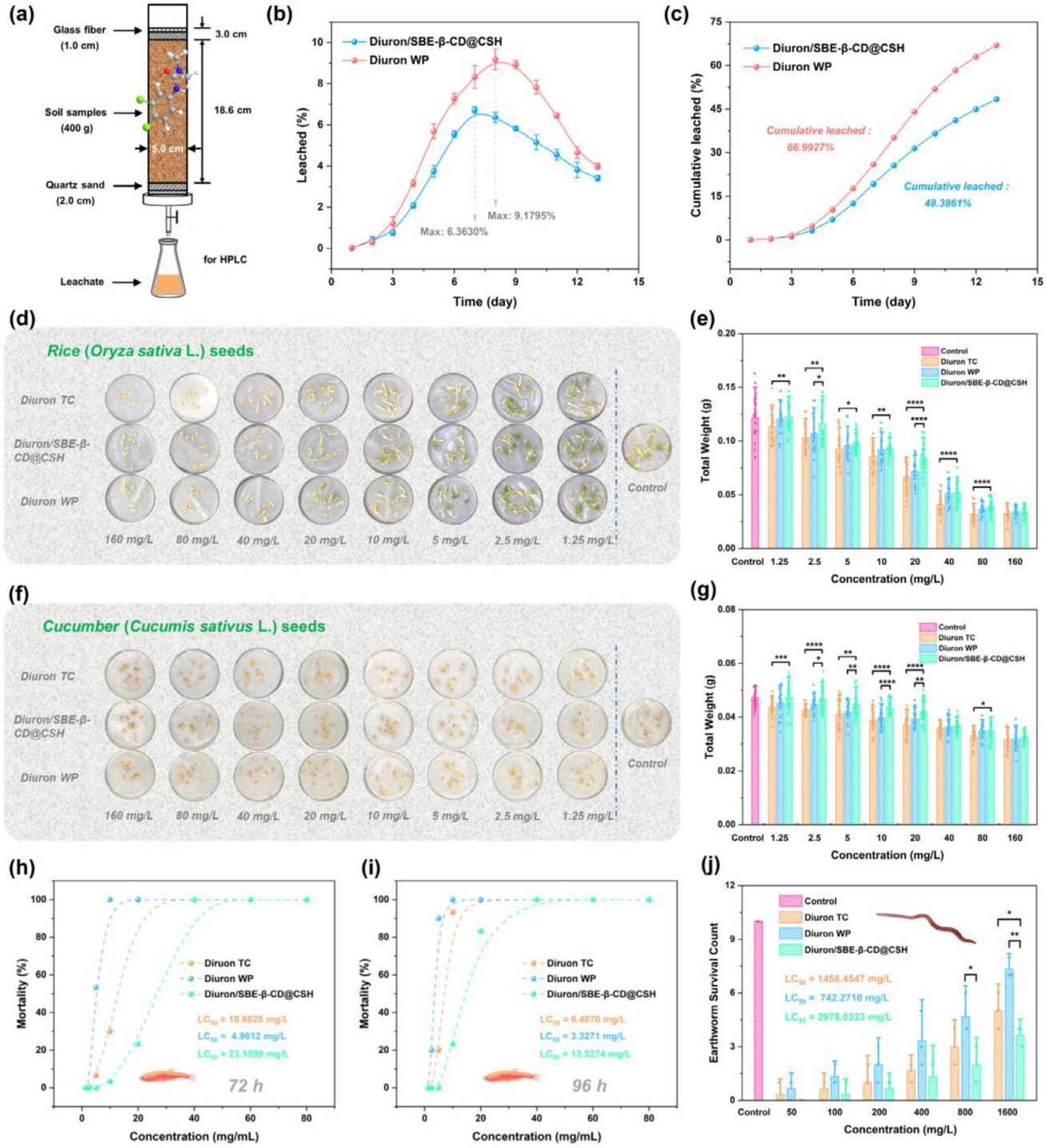


FIGURE 7 | Leaching behavior and nontarget safety assessment of the formulations. (a) Schematic illustration of the soil column leaching experimental setup. (b, c) Breakthrough curves (b) and cumulative leaching curves (c) for Diuron WP and Diuron/SBE-β-CD@CSH in soil columns. Independent experiments: $n = 3$; the data are presented as mean ± standard deviation. (d, e) Germination status (d) and fresh weights (e) of cucumber seeds after 1 week of treatment with various concentrations of Diuron TC, Diuron WP, and Diuron/SBE-β-CD@CSH. Number of measurements: $n = 10$ across three independent experiments; the data are presented as mean ± standard deviation. (f, g) Germination status (f) and fresh weights (g) of rice seeds treated similarly for 1 week. Number of measurements: $n = 10$ across three independent experiments; the data are presented as mean ± standard deviation. (h, i) Mortality rates of zebrafish after exposure to varying concentrations of Diuron TC, Diuron WP, and Diuron/SBE-β-CD@CSH for 72 h (h) and 96 h (i). Number of measurements: $n = 10$ across three independent experiments; the data are presented as mean ± standard deviation. (j) Survival rates of earthworms after 48 h of treatment with different concentrations of Diuron TC, Diuron WP, and Diuron/SBE-β-CD@CSH. Number of measurements: $n = 10$ across three independent experiments; the data are presented as mean ± standard deviation.

At increased herbicide concentrations, germination rates exhibited pronounced differences. At 40 mg/L, cucumber seed germination was reduced to 56.67% in the Diuron TC group and 83.33% in the Diuron WP group, whereas Diuron/SBE-β-CD@CSH maintained a higher germination rate of 93.33%, clearly indicating reduced phytotoxicity (Figure S12). These differences intensified at elevated concentrations: at 80 and 160 mg/L, Diuron TC completely inhibited germination in both crops, while Diuron WP fully inhibited cucumber germination and drastically reduced rice germination (90.00% at 80 mg/L; 10.00% at 160 mg/L; Figure S13). In contrast, Diuron/SBE-β-CD@CSH substantially mitigated these toxic effects, maintaining partial germination even at the highest concentration tested (23.33% for cucumber and 36.67% for rice), despite expected dose-dependent phytotoxicity. Notably, at the highest tested concentration (160 mg/L), no significant differences in total biomass were observed across treatments, indicating universal suppression of plant development under excessive herbicide levels.

Throughout the exposure period, Diuron WP consistently exhibited the highest acute toxicity to adult zebrafish (*Danio rerio*), followed by Diuron TC, whereas Diuron/SBE-β-CD@CSH demonstrated the lowest toxicity, as evidenced by consistently higher LC_{50} values. At 24 h, the LC_{50} values were 32.17 mg/L for Diuron WP, 53.18 mg/L for Diuron TC, and 58.11 mg/L for Diuron/SBE-β-CD@CSH, reflecting toxicity reductions of 80.66% and 9.27% relative to the former two formulations, respectively. This trend was further amplified with prolonged exposure. By 72 h, the LC_{50} value of Diuron/SBE-β-CD@CSH increased by 366.76% and 117.18% compared to Diuron TC and Diuron WP, respectively (Figure 7h). At 96 h, Diuron WP exhibited the greatest toxicity, with an LC_{50} of only 3.33 mg/L, whereas Diuron/SBE-β-CD@CSH reduced toxicity approximately fourfold (Figure 7i).

Earthworms (*Eisenia fetida*) are widely recognized as indicator species for evaluating soil ecotoxicity. In this study, the filter paper contact method was employed to assess the acute toxicity. Diuron exposure is known to induce severe toxicological effects, including cellular damage, oxidative stress, tissue necrosis, histopathological alterations, and genotoxicity [77]. Within 48 h of exposure, earthworms exhibited acute stress responses, such as convulsions, rolling behavior, magenta-colored blood excretion, and eventual body fragmentation (Figure S12). Mortality data revealed that Diuron WP posed the highest toxicity, with an LC_{50} of 742.27 mg/L, followed by Diuron TC at 1458.45 mg/L. In notable contrast, Diuron/SBE-β-CD@CSH demonstrated the lowest toxicity, with an LC_{50} of 2978.03 mg/L, indicating nearly a threefold reduction compared to Diuron WP (Figure 7j). This marked reduction is primarily attributed to the dual encapsulation of Diuron molecules and the absence of potentially harmful surfactants and dispersants typically present in commercial formulations. Together, these ecotoxicological findings from aquatic, soil, and crop-related assays consistently confirm the superior safety profile of Diuron/SBE-β-CD@CSH toward nontarget organisms, supporting its potential as a safer herbicide formulation.

2.6 | In Vitro Cytotoxicity and ROS Generation

Diuron has been previously implicated in hepatotoxicity and cardiotoxicity [78, 79]. To further investigate its biotoxic potential, myocardial (AC16) and hepatic (MIHA) cell lines were exposed to various concentrations of Diuron formulations. As illustrated in Figure 8a,b, cell viability decreased dose-dependently, with Diuron WP demonstrating the highest cytotoxicity at equivalent concentrations. Specifically, at 96 mg/L, MIHA and AC16 cell viability decreased drastically to below 56% and 12%, respectively, in the Diuron WP treatment group. In contrast, viability in the Diuron/SBE-β-CD@CSH group remained substantially higher at 83% and 43%, respectively. Time-dependent cytotoxicity was similarly notable; after 72 h, MIHA cell viability in Diuron TC and Diuron WP groups decreased below 40%, whereas Diuron/SBE-β-CD@CSH-treated cells-maintained viability above 50%. Comparable trends were observed in AC16 cells (Figure 8c,d). Live/dead cell assays provided further confirmation, revealing significantly fewer dead cells (indicated by red fluorescence) in Diuron/SBE-β-CD@CSH-treated groups compared with other formulations (Figure 8f), indicative of reduced cytotoxicity following assembly with chitosan and SBE-β-CD. Given that Diuron-induced cytotoxicity is partially mediated by reactive oxygen species (ROS) [80, 81], intracellular ROS production was quantified after 12 h of treatment. ROS levels were significantly elevated in the Diuron WP group, exceeding 2.5-fold of control values. In contrast, both Diuron TC and Diuron/SBE-β-CD@CSH formulations exhibited reduced ROS production, with the latter demonstrating the most pronounced antioxidant effect (Figure 8e–g). This reduction in oxidative stress may be attributed to the nanoparticle encapsulation mitigating direct cellular exposure to Diuron and the presence of chitosan-derived hydroxyl and amino groups, known for their efficacy in scavenging free radicals and suppressing oxidative damage [82].

In addition, SBE-β-CD is a biocompatible pharmaceutical excipient capable of forming inclusion complexes with hydrophobic molecules. It is therefore reasonable to hypothesize that such complexation reduces the readily bioavailable fraction of Diuron in the exposure medium, thereby attenuating its acute interactions with cellular membranes and mitochondria [83, 84]. Moreover, incorporation into a chitosan-based polysaccharide matrix is expected to further physically confine the active ingredient within a carrier network. Although the free-drug fraction and release kinetics were not directly quantified in the present study, carrier-mediated moderation of immediate exposure has been widely reported for polysaccharide-based delivery systems [84]. Consistent with our ROS-related observations, chitosan and its derivatives have been reported to exhibit intrinsic antioxidant and free-radical scavenging activities, primarily attributed to the presence of hydroxyl and amino functional groups, which may further mitigate oxidative stress [85, 86]. Collectively, the higher cell viability, reduced proportion of dead cells, and markedly lower intracellular ROS levels observed in Diuron/SBE-β-CD@CSH-treated AC16 and MIHA cells support the notion that the nanocarrier formulation exhibits reduced cytotoxicity toward mammalian cardiac and hepatic cells.

2.7 | In Vivo Safety Evaluation in a Rat Model

To further evaluate the safety profile of Diuron/SBE-β-CD@CSH, an in vivo toxicity assessment was conducted in rats administered daily oral treatments over 32 days. Initially, body weights across all groups were comparable; however, over time, significantly

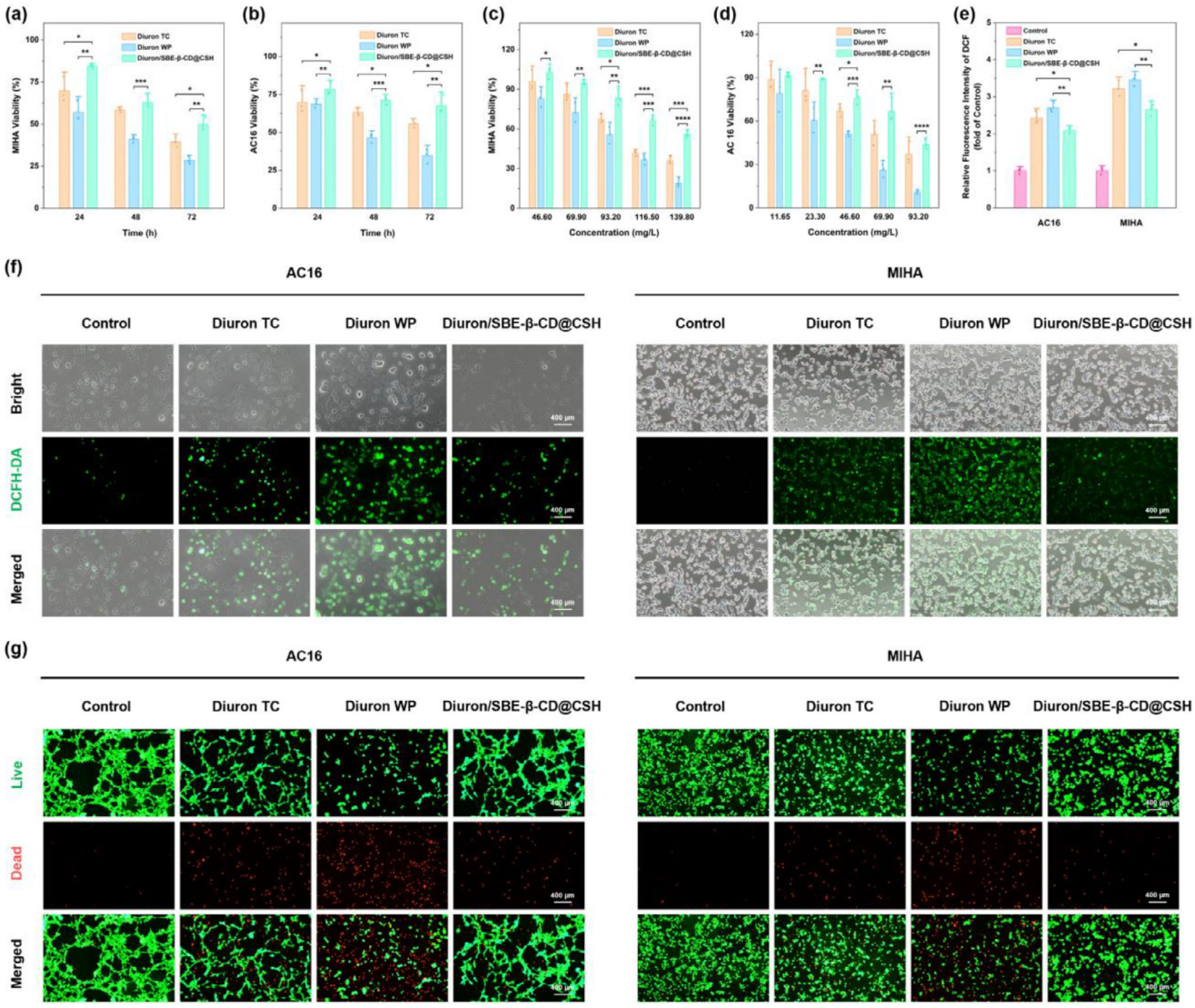


FIGURE 8 | Evaluation of safety in cell models. (a, b) Viability of MIHA (a) and AC16 (b) cells after treatment with various concentrations of Diuron TC, Diuron WP, and Diuron/SBE-β-CD@CSH. Number of independent experiments: $n = 3$; the data are presented as mean ± standard deviation. (c, d) Time-dependent cytotoxicity of MIHA (c) and AC16 (d) cells after exposure to Diuron TC, Diuron WP, and Diuron/SBE-β-CD@CSH at 400 μmol/L and 200 μmol/L, respectively. Number of independent experiments: $n = 3$; the data are presented as mean ± standard deviation. (e, f) Quantitative analysis (e) and fluorescence images (f) of intracellular ROS levels in AC16 and MIHA cells after 12 h of exposure to Diuron TC, Diuron WP, and Diuron/SBE-β-CD@CSH. Number of independent experiments: $n = 3$; the data are presented as mean ± standard deviation. (g) Live/dead cell staining images of AC16 and MIHA cells after 24 h of coincubation with Diuron TC, Diuron WP, and Diuron/SBE-β-CD@CSH.

greater weight gains occurred in control and Diuron/SBE-β-CD@CSH groups compared with Diuron TC and Diuron WP groups, the latter showing the least increase (Figure 9a). Hepatotoxicity, assessed through serum alanine aminotransferase (ALT) and aspartate aminotransferase (AST) levels, was markedly elevated in Diuron TC and Diuron WP groups. Specifically, Diuron WP displayed the highest ALT (82.124 U/L) and AST (207.810 U/L) values, aligning with previous findings (Figure 9b) [79], and exceeding the upper limits of the normal reference ranges for Sprague-Dawley rats (Table S6). Conversely, Diuron/SBE-β-CD@CSH treatment significantly reduced ALT and AST by approximately 20%, keeping these parameters within or close to the normal reference ranges for rats, indicative of enhanced hepatoprotection. Cardiac toxicity, indicated by elevated creatine kinase (CK) and lactate dehydrogenase (LDH) levels, was severe in the Diuron WP group, where CK and LDH reached approximately twice (CK: 2.00-fold; LDH: 1.74-fold) those observed in controls (Figure 9c). The mean CK and LDH activities in the Diuron WP group (975.390 and 1118.925 U/L, respectively) exceeded the upper limits of the normal reference ranges for rats, whereas the corresponding control values (CK 488.795 U/L and LDH 642.003 U/L) remained within these reference intervals (Table S6). Although substantial cardiac damage also occurred in the Diuron TC group, Diuron/SBE-β-CD@CSH significantly mitigated this effect, reducing CK and LDH levels by around 28%, nearly restoring them to control values. Renal toxicity was minimal, as indicated by reduced blood urea nitrogen (BUN) in the Diuron WP group, likely reflecting impaired hepatic urea synthesis rather than direct kidney injury, with negligible changes in creatinine (CREA) levels (Figure 9d). Hematological

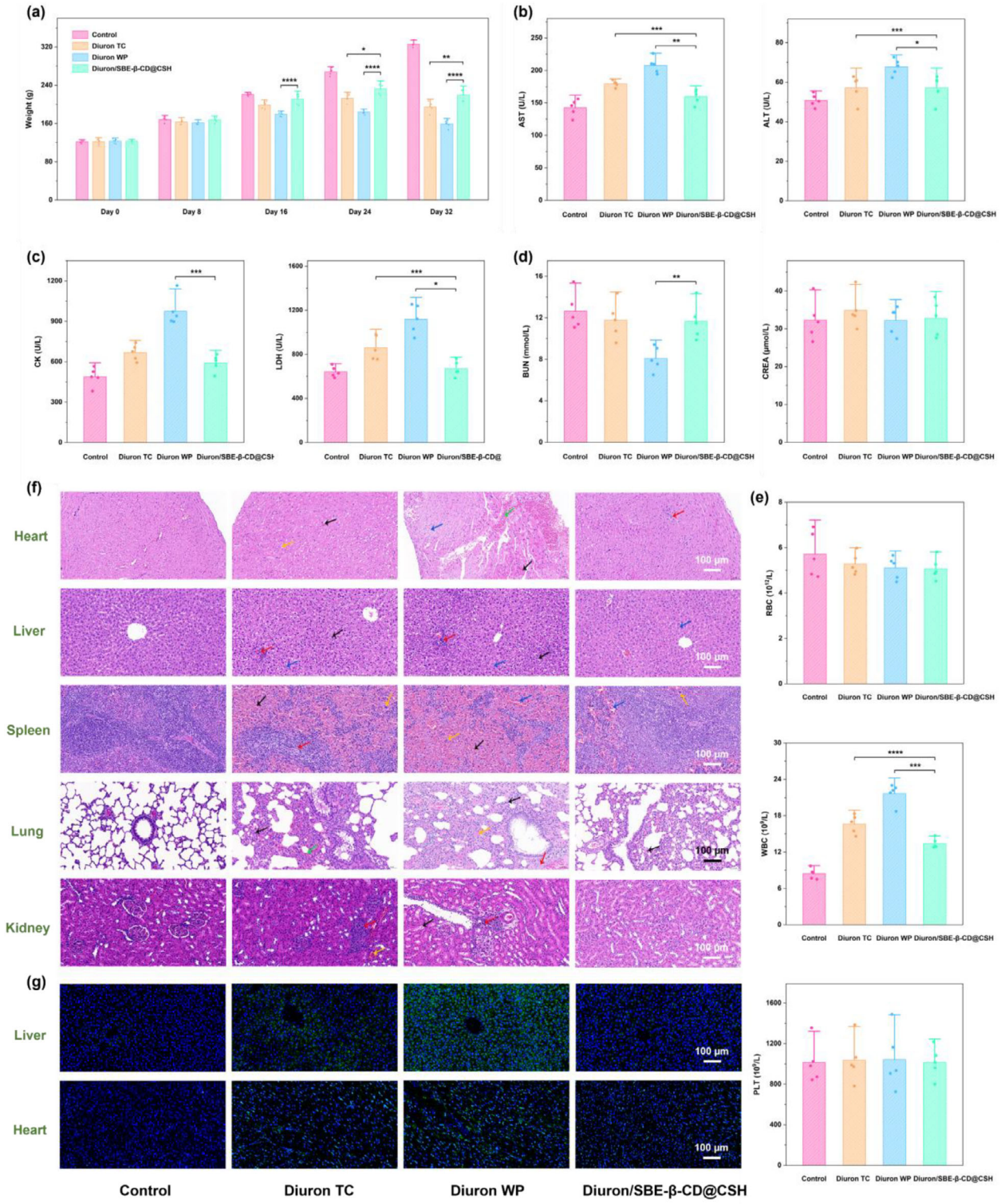


FIGURE 9 | Safety evaluation of Diuron formulations in rat models. (a) Weekly body weight changes in rats following daily oral administration of Diuron TC, Diuron WP, and Diuron/SBE-β-CD@CSH. Number of measurements: $n = 5$ across three independent experiments; the data are presented as mean ± standard deviation. (b) Quantitative analysis of liver function biomarkers (AST and ALT) in rat blood after 32 days of daily oral administration of Diuron TC, Diuron WP, and Diuron/SBE-β-CD@CSH. Number of measurements: $n = 5$ across three independent experiments; the data are presented as mean ± standard deviation. (c) Quantitative analysis of myocardial function biomarkers (CK and LDH). Number of measurements: $n = 5$ across three independent experiments; the data are presented as mean ± standard deviation. (d) Quantitative analysis of kidney function biomarkers (BUN and CREA). Number of measurements: $n = 5$ across three independent experiments; the data are presented as mean ± standard deviation. (e) Quantitative analysis of RBC, WBC, and PLT. Number of measurements: $n = 5$ across three independent experiments; the data are presented as mean ± standard deviation. (f) H&E staining images of rat heart, liver, spleen, lung, and kidney tissues following 32-day treatment. (g) Fluorescence images of 4-HNE staining in rat heart and liver tissues.

analyses revealed no significant variations in platelet (PLT) and red blood cell (RBC) counts among treatments. However, white blood cell (WBC) counts, indicative of inflammation, were lowest in controls and significantly lower in the Diuron/SBE-β-CD@CSH group (1.59-fold relative to controls) compared to Diuron TC (1.97-fold) and Diuron WP (2.57-fold), suggesting attenuated inflammatory responses and overall reduced systemic toxicity (Figure 9e).

Histopathological examination by hematoxylin–eosin staining (Figure 9f) demonstrated intact tissue morphology in the control group. In contrast, the Diuron TC group exhibited extensive organ damage, characterized by myocardial vacuolation (orange arrows) and necrosis (black arrows); hepatocyte edema (blue arrows), cytoplasmic loosening, nuclear pyknosis (black arrows), and lymphocytic infiltration within portal areas (red arrows); splenic lymphocyte necrosis (red arrows), severe congestion in splenic red pulp (black arrows), and occasional multinucleated giant cells (orange arrows); granulocyte infiltration within alveoli (black arrows), vascular wall thickening accompanied by minor hemorrhages (green arrows); and renal multifocal inflammation (red arrows) with interstitial vascular congestion (orange arrows). Toxicity intensified markedly in the Diuron WP group, characterized by pronounced myocardial cytoplasmic disintegration (blue arrows), uneven myocardial fiber staining, and focal interstitial hemorrhages (green arrows). Hepatic damage was exacerbated, evidenced by severe hepatocyte injury, prominent sinusoidal congestion in the spleen (blue arrows), alveolar necrosis with marked granulocyte infiltration, pronounced thickening of vascular walls (red arrows), and presence of alveolar foam cells and eosinophilic material deposits (orange arrows). Renal histopathology indicated significant eosinophilic tubular deposits (black arrows) and extensive lymphocytic infiltration. In stark contrast, Diuron/SBE-β-CD@CSH treatment resulted in minimal histological changes, restricted primarily to mild myocardial lymphocyte infiltration (red arrows) and slight edema across other organs, indicative of reduced inflammatory responses and preserved tissue integrity.

Given prior evidence that Diuron/SBE-β-CD@CSH reduces oxidative stress and cytotoxicity, we further assessed these protective effects in vivo via 4-hydroxy-2-nonenal (4-HNE) fluorescence staining, a marker of lipid peroxidation and oxidative damage [87]. As depicted in Figure 9g, minimal 4-HNE fluorescence was observed in control tissues, reflecting negligible oxidative injury, whereas maximal fluorescence intensity, indicative of severe oxidative stress, occurred in the Diuron WP group. Moderate oxidative damage was noted in the Diuron TC group. Crucially, Diuron/SBE-β-CD@CSH markedly reduced fluorescence intensity, confirming substantial antioxidant capacity consistent with cellular studies. Taken together with the in vitro findings, the coordinated reductions in intracellular ROS and tissue 4-hydroxynonenal (4-HNE) levels suggest that Diuron/SBE-β-CD@CSH attenuates oxidative stress-associated injury in vivo. This interpretation is consistent with the observed mitigation of ALT/AST and CK/LDH alterations, as well as the overall milder histopathological changes [85, 86]. Although Diuron bioavailability, release kinetics, and tissue distribution were not directly quantified in the present study, the improved biocompatibility may plausibly be attributed to carrier-mediated modulation of effective exposure, together with the antioxidant and free-radical scavenging capacities reported for chitosan-based systems and cyclodextrin-enabled complexation [83–86]. Collectively, these findings indicate that Diuron/SBE-β-CD@CSH can attenuate Diuron-associated toxicity at both cellular and systemic levels under the experimental conditions examined, while also exhibiting improved environmental behavior, such as reduced mobility and nontarget toxicity, compared with conventional formulations. However, potential long-term environmental impacts associated with repeated applications, including cumulative soil interactions and ecosystem-level effects, warrant further investigation through multiseason field studies.

3 | Conclusions

In this study, we developed an efficacious and biocompatible herbicide nanoformulation, Diuron/SBE-β-CD@CSH, via a hierarchical self-assembly strategy. Initially, Diuron molecules formed inclusion complexes with SBE-β-CD through host–guest molecular recognition, followed by electrostatic self-assembly with chitosan to yield uniformly sized nanoparticles. Compared to commercial Diuron WP, these nanoparticles exhibited stimuli-responsive controlled release characteristics sensitive to temperature and pH, as well as enhanced photostability owing to effective photon-shielding mechanisms. Additionally, the coassembled nanoparticles displayed superior dynamic deposition and exceptional rainfastness on weed leaf surfaces. Their nanoscale dimensions and excellent biocompatibility facilitated efficient absorption via leaf and root pathways, ensuring effective bidirectional systemic translocation within plant tissues. Without introducing additional formulation components, Diuron/SBE-β-CD@CSH nanoparticles demonstrated markedly improved control efficacy against broadleaf weeds (*Chenopodium serotinum* L. and *Abutilon theophrasti* Medicus) and grassy weeds (*Setaria faberi* R. A. W. Herrmann) in both greenhouse and field trials compared to commercial WP. Comprehensive toxicity evaluations using multiple nontarget organism models, including crop species (cucumber and rice), aquatic organisms (zebrafish), soil organisms (earthworms), in vitro cell lines (AC16 and MIHA), and in vivo rat models, revealed enhanced ecological and biological safety profiles relative to both Diuron technical and Diuron WP formulations. This coassembled nanoherbicide platform exhibits significant promise for sustainable and efficient agricultural management, characterized by simple preparation procedures, minimized environmental loss, enhanced target-specific herbicidal activity, and substantially improved ecological safety. Thus, it offers a compelling strategy for promoting agricultural sustainability and environmental stewardship in future weed management practices.

Acknowledgments

This work is financially supported by the University Synergy Innovation Program of Anhui Province (GXXT-2021-059), the National Key Research and Development Program of China (2023YFD1702102), and the Major Natural Science Research Project of Anhui Universities (2023AH040143).

Ethics Statement

All animal experiments were conformed to the guidelines for the care and use of laboratory animals and ethically approved by the Laboratory

Animal Ethics Committee of the Anhui Agriculture University (Protocol number AHAU2022012).

Conflicts of Interest

The authors declare no conflicts of interest.

Data Availability Statement

The data that support the findings of this study are available from the corresponding author upon reasonable request.

References

1. D. Tilman, K. G. Cassman, P. A. Matson, R. Naylor, and S. Polasky, "Agricultural Sustainability and Intensive Production Practices," *Nature* 418 (2002): 671–677.

2. C. Lamberth, S. Jeanmart, T. Luksch, and A. Plant, "Current Challenges and Trends in the Discovery of Agrochemicals," *Science* 341 (2013): 742–746.

3. B. Borel, "CRISPR, Microbes and More Are Joining the War Against Crop Killers," *Nature* 543 (2017): 302–304.

4. F. Maggi, F. H. M. Tang, D. la Cecilia, and A. McBratney, "PEST-CHEMGRIDS, Global Gridded Maps of the Top 20 Crop-Specific Pesticide Application Rates From 2015 to 2025," *Scientific Data* 6 (2019): 170.

5. C. J. Swanton and S. F. Weise, "Integrated Weed Management: The Rationale and Approach," *Weed Technology* 5 (1991): 657–663.

6. A. Parven, I. M. Meftaul, K. Venkateswarlu, and M. Megharaj, "Herbicides in Modern Sustainable Agriculture: Environmental Fate, Ecological Implications, and human Health Concerns," *International Journal of Environmental Science and Technology* 22 (2024): 1181–1202.

7. A. M. Sharkey, B. J. Williams, and K. M. Parker, "Herbicide Drift From Genetically Engineered Herbicide-Tolerant Crops," *Environmental Science & Technology* 55 (2021): 15559–15568.

8. A. Cerdà, I. N. Daliakopoulos, E. Terol, et al., "Long-Term Monitoring of Soil Bulk Density and Erosion Rates in Two *Prunus persica* (L) Plantations Under Flood Irrigation and Glyphosate Herbicide Treatment in La Ribera District, Spain," *Journal of Environmental Management* 282 (2021): 111965.

9. R. M. de Souza, D. Seibert, H. B. Quesada, F. de Jesus Bassetti, M. R. Fagundes-Klen, and R. Bergamasco, "Occurrence, Impacts and General Aspects of Pesticides in Surface Water: A Review," *Process Safety and Environmental Protection* 135 (2020): 22–37.

10. S. T. Dugan, A. Muhammetoglu, and A. Uslu, "A Combined Approach for the Estimation of Groundwater Leaching Potential and Environmental Impacts of Pesticides for Agricultural Lands," *Science of the Total Environment* 901 (2023): 165892.

11. M. Kah, R. S. Kookana, A. Gogos, and T. D. Bucheli, "A Critical Evaluation of Nanopesticides and Nanofertilizers Against Their Conventional Analogues," *Nature Nanotechnology* 13 (2018): 677–684.

12. A. Varah, K. Ahodo, S. R. Coutts, et al., "The Costs of Human-Induced Evolution in an Agricultural System," *Nature Sustainability* 3 (2020): 63–71.

13. F. Gomollón-Bel, "Ten Chemical Innovations That Will Change Our World: IUPAC Identifies Emerging Technologies in Chemistry With Potential to Make Our Planet More Sustainable," *Chemistry International* 41 (2019): 12–17.

14. W. Shangguan, Q. Huang, H. Chen, et al., "Making the Complicated Simple: A Minimizing Carrier Strategy on Innovative Nanopesticides," *Nano-Micro Letters* 16 (2024): 193.

15. K. Ariga, X. Jia, J. Song, et al., "Nanoarchitectonics Beyond Self-Assembly: Challenges to Create Bio-Like Hierarchic Organization," *Angewandte Chemie International Edition* 59 (2020): 15424–15446.

16. Z. Liu, W. Lin, and Y. Liu, "Macrocyclic Supramolecular Assemblies Based on Hyaluronic Acid and Their Biological Applications," *Accounts of Chemical Research* 55 (2022): 3417–3429.

17. Y. Xiao, C. Wu, M. Han, P. Chen, L. Zhou, and Q. Yin, "Advanced Supramolecular Self-Assembly for Lifecycle-Optimized Agrochemical Delivery," *Coordination Chemistry Reviews* 516 (2024): 215953.

18. S. Mann, "Self-Assembly and Transformation of Hybrid Nano-Objects and Nanostructures Under Equilibrium and Non-Equilibrium Conditions," *Nature Materials* 8 (2009): 781–792.

19. P. H. Shan, J. H. Hu, M. Liu, Z. Tao, X. Xiao, and C. Redshaw, "Progress in Host–Guest Macrocycle/Pesticide Research: Recognition, Detection, Release and Application," *Coordination Chemistry Reviews* 467 (2022): 214580.

20. Y. Xiao, C. Wu, P. Cui, L. Zhou, and Q. Yin, "Pursuing Green and Efficient Agriculture From Molecular Assembly: A Review of Solid-State Forms on Agrochemicals," *Journal of Agricultural and Food Chemistry* 71 (2023): 10500–10524.

21. L. Luo, G. Nie, D. Tian, H. Deng, L. Jiang, and H. Li, "Dynamic Self-Assembly Adhesion of a Paraquat Droplet on a Pillar[5]Arene Surface," *Angewandte Chemie International Edition* 55 (2016): 12713–12716.

22. S. Gao, J. Jiang, X. Li, F. Ye, Y. Fu, and L. Zhao, "An Environmentally Safe Formulation With Enhanced Solubility and Fungicidal Activity: Self-Assembly and Characterization of Difenoconazole-β-CD Inclusion Complex," *Journal of Molecular Liquids* 327 (2021): 114874.

23. W. Li, W. Xu, S. Zhang, et al., "Supramolecular Biopharmaceutical Carriers Based on Host–Guest Interactions," *Journal of Agricultural and Food Chemistry* 70 (2022): 12746–12759.

24. Q. Ji, X. Mu, D. Hu, et al., "Fabrication of Host–Guest Complexes Between Adamantane-Functionalized 1,3,4-Oxadiazoles and β-Cyclodextrin With Improved Control Efficiency Against Intractable Plant Bacterial Diseases," *ACS Applied Materials & Interfaces* 14 (2022): 2564–2577.

25. C. Gao, Q. Huang, Q. Lan, et al., "A User-Friendly Herbicide Derived From Photo-Responsive Supramolecular Vesicles," *Nature Communications* 9 (2018): 2967.

26. J. Yang, H. Ye, H. Xiang, et al., "Photo-Stimuli Smart Supramolecular Self-Assembly of Azobenzene/β-Cyclodextrin Inclusion Complex for Controlling Plant Bacterial Diseases," *Advanced Functional Materials* 33 (2023): 2303206.

27. J. Yang, K. Liu, Y. Chen, et al., "A Supramolecular Bactericidal Material for Preventing and Treating Plant-Associated Biofilms," *Nature Communications* 16 (2025): 2627.

28. A. Ciesielski, C. Palma, M. Bonini, and P. Samorì, "Towards Supramolecular Engineering of Functional Nanomaterials: Pre-Programming Multi-Component 2D Self-Assembly at Solid-Liquid Interfaces," *Advanced Materials* 22 (2010): 3506–3520.

29. H. Qiu, Z. M. Hudson, M. A. Winnik, and I. Manners, "Multidimensional Hierarchical Self-Assembly of Amphiphilic Cylindrical Block Comicelles," *Science* 347 (2015): 1329–1332.

30. Y. Lu, J. Lin, L. Wang, L. Zhang, and C. Cai, "Self-Assembly of Copolymer Micelles: Higher-Level Assembly for Constructing Hierarchical Structure," *Chemical Reviews* 120 (2020): 4111–4140.

31. W. Shi, S. Li, X. Wang, S. Li, X. Zhang, and F. Hou, "An Electrostatic Self-Assembly Approach to Prepare Tebuconazole Nanoparticles With Improved Sustained Release and Enhanced Antifungal Activity," *Colloids and Surfaces B: Biointerfaces* 216 (2022): 112587.

32. C. He, S. Liu, Y. Zhang, et al., "Multi-Mechanism Encapsulation in a Bio-Stimulant-Based Smart Nanocarrier Enhances *Fusarium* Head Blight Control Through Synergistic Action and Triggered Release," *Advanced Functional Materials* 35 (2025): 2506319.

33. C. V. Pardeshi, R. V. Kothawade, A. R. Markad, et al., "Sulfobutylether-β-Cyclodextrin: A Functional Biopolymer for Drug Delivery Applications," *Carbohydrate Polymers* 301 (2023): 120347.

34. W. Lai, A. L. Rogach, and W. Wong, "Chemistry and Engineering of Cyclodextrins for Molecular Imaging," *Chemical Society Reviews* 46 (2017): 6379–6419.

35. J. Huang, X. Wang, T. Huang, et al., "Application of Sodium Sulfobutylether-β-Cyclodextrin Based on Encapsulation," *Carbohydrate Polymers* 333 (2024): 121985.

36. A. Douhal, "Ultrafast Guest Dynamics in Cyclodextrin Nanocavities," *Chemical Reviews* 104 (2004): 1955–1976.

37. R. Periasamy, S. Kothainayaki, R. Rajamohan, and K. Sivakumar, "Spectral Investigation and Characterization of Host–Guest Inclusion Complex of 4,4′-Methylene-Bis(2-Chloroaniline) With Beta-Cyclodextrin," *Carbohydrate Polymers* 114 (2014): 558–566.

38. B. Liu, W. Li, J. Zhao, Y. Liu, X. Zhu, and G. Liang, "Physicochemical Characterisation of the Supramolecular Structure of Luteolin/Cyclodextrin Inclusion Complex," *Food Chemistry* 141 (2013): 900–906.

39. F. Liu, J. Antoniou, Y. Li, et al., "Chitosan/Sulfobutylether-β-Cyclodextrin Nanoparticles as a Potential Approach for Tea Polyphenol Encapsulation," *Food Hydrocolloids* 57 (2016): 291–300.

40. A. A. Mahmoud, G. S. El-Feky, R. Kamel, and G. E. Awad, "Chitosan/Sulfobutylether-β-Cyclodextrin Nanoparticles as a Potential Approach for Ocular Drug Delivery," *International Journal of Pharmaceutics* 413 (2011): 229–236.

41. Y. Shen, C. An, J. Jiang, et al., "Temperature-Dependent Nanogel for Pesticide Smart Delivery With Improved Foliar Dispersion and Bioactivity for Efficient Control of Multiple Pests," *ACS Nano* 16 (2022): 20622–20632.

42. C. An, B. Huang, J. Jiang, et al., "Design and Synthesis of a Water-Based Nanodelivery Pesticide System for Improved Efficacy and Safety," *ACS Nano* 18 (2024): 662–679.

43. D. Huang, H. Qi, H. Liu, F. Yuan, C. Yang, and T. Liu, "Two Birds With One Stone: Eco-Friendly Nano-Formulation Endows a Commercial Fungicide With Excellent Insecticidal Activity," *Advanced Functional Materials* 35 (2025): 2420401.

44. P. Gao, Z. Zhang, J. Shen, et al., "Weed Seed Bank Dynamics Responses to Long-Term Chemical Control in a Rice–Wheat Cropping System," *Pest Management Science* 76 (2020): 1993–2003.

45. T. Li, J. Fan, Z. Qian, et al., "Predation on Weed Seeds and Seedlings by *Pheretima guillelmi* and Its Potential for Weed Biocontrol," *Weed Science* 68 (2020): 639–645.

46. S. Singh, A. Singh, S. S. Hallan, A. Brangule, B. Kumar, and R. Bhatia, "A Compiled Update on Nutrition, Phytochemicals, Processing Effects, Analytical Testing and Health Effects of Chenopodium Album: A Non-Conventional Edible Plant (NCEP)," *Molecules* 28 (2023): 4902.

47. Y. Xiao, C. Wu, S. Feng, et al., "Green and Efficient Delivery of Pesticides Throughout Their Life Cycle via Cooperative Solid and Solution Self-Assembly," *Chemical Engineering Journal* 475 (2023): 146037.

48. F. Gambinossi, S. E. Mylon, and J. K. Ferri, "Aggregation Kinetics and Colloidal Stability of Functionalized Nanoparticles," *Advances in Colloid and Interface Science* 222 (2015): 332–349.

49. J. Xu, Y. Zhang, X. Li, and Y. Zheng, "Inclusion Complex of Nateglinide With Sulfobutyl Ether β-Cyclodextrin: Preparation, Characterization and Water Solubility," *Journal of Molecular Structure* 1141 (2017): 328–334.

50. M. Liu, A. Chen, Y. Wang, C. Wang, B. Wang, and D. Sun, "Improved Solubility and Stability of 7-Hydroxy-4-Methylcoumarin at Different Temperatures and pH Values Through Complexation With Sulfobutyl Ether-β-Cyclodextrin," *Food Chemistry* 168 (2015): 270–275.

51. C. Qin, H. Li, Q. Xiao, Y. Liu, J. Zhu, and Y. Du, "Water-Solubility of Chitosan and Its Antimicrobial Activity," *Carbohydrate Polymers* 63 (2006): 367–374.

52. K. I. Matshetshe, S. Parani, S. M. Manki, and O. S. Oluwafemi, "Preparation, Characterization and In Vitro Release Study of β-Cyclodextrin/Chitosan Nanoparticles Loaded *Cinnamomum zeylanicum* Essential Oil," *International Journal of Biological Macromolecules* 118 (2018): 676–682.

53. Y. Xiang, X. Lu, J. Yue, et al., "Stimuli-Responsive Hydrogel as Carrier for Controlling the Release and Leaching Behavior of Hydrophilic Pesticide," *Science of the Total Environment* 722 (2020): 137811.

54. L. Su, J. D. Sivey, and N. Dai, "Emerging Investigator Series: Sunlight Photolysis of 2,4-D Herbicides in Systems Simulating Leaf Surfaces," *Environmental Science: Processes & Impacts* 20 (2018): 1123–1135.

55. M. Song, J. Ju, S. Luo, et al., "Controlling Liquid Splash on Superhydrophobic Surfaces by a Vesicle Surfactant," *Science Advances* 3 (2017): e1602188.

56. H. Xie, G. Yu, X. Wang, et al., "Sea Urchin-Like Nanocarrier for Enhancing Pesticide Retention and Rain Fastness on Hydrophobic and Hydrophilic Crop Foliage," *Chemical Engineering Journal* 490 (2024): 151901.

57. N. Mohd Yusof, J. Jai, and F. Hamzah, "Effect of Coating Materials on the Properties of Chitosan-Starch-Based Edible Coatings," *IOP Conference Series: Materials Science and Engineering* 507 (2019): 012011.

58. N. Calero, J. Muñoz, P. Ramírez, and A. Guerrero, "Flow Behaviour, Linear Viscoelasticity and Surface Properties of Chitosan Aqueous Solutions," *Food Hydrocolloids* 24 (2010): 659–666.

59. K. Wei, Z. Li, Z. Zheng, et al., "Natural Glycyrrhizic Acid-Tailored Nanoparticles Toward the Enhancement of Pesticide Bioavailability," *Advanced Functional Materials* 34 (2024): 2315493.

60. C. Richard Glass, K. F. Walters, P. H. Gaskell, et al., "Recent Advances in Computational Fluid Dynamics Relevant to the Modelling of Pesticide Flow on Leaf Surfaces," *Pest Management Science* 66 (2010): 2–9.

61. W. Qiu, H. Guo, H. Zheng, et al., "CFD Modelling to Analyze the Droplets Deposition Behavior on Vibrating Rice Leaves," *Computers and Electronics in Agriculture* 201 (2022): 107330.

62. Y. Xiao, C. Wu, Y. Liu, L. Zhou, S. Wu, and Q. Yin, "Biocompatible Nano-Cocrystal Engineering for Targeted Herbicide Delivery: Enhancing Efficacy Through Stimuli-Responsive Release and Reduced Environmental Losses," *ACS Applied Materials & Interfaces* 16 (2024): 51283–51300.

63. H. Krähmer, H. Walter, P. Jeschke, K. Haaf, P. Baur, and R. Evans, "What Makes a Molecule a Pre- or a Post-Herbicide—How Valuable Are Physicochemical Parameters for Their Design?," *Pest Management Science* 77 (2021): 4863–4873.

64. H. Lundegårdh, "The Influence of Diuron [3-(3,4-Dichlorophenyl)-1,1-Dimethylurea] on the Respiratory and Photosynthetic Systems of Plants," *Proceedings of the National Academy of Sciences of United States of America* 53 (1965): 703–710.

65. F. Sicbaldi, G. A. Sacchi, M. Trevisan, and A. A. M. Del Re, "Root Uptake and Xylem Translocation of Pesticides From Different Chemical Classes," *Pesticide Science* 50 (1997): 111–119.

66. M. D. Devine and L. M. Hall, "Implications of Sucrose Transport Mechanisms for the Translocation of Herbicides," *Weed Science* 38 (1990): 299–304.

67. H. B. Currier and C. D. Dybing, "Foliar Penetration of Herbicides: Review and Present Status," *Weeds* 7 (1959): 195.

68. P. Wang, E. Lombi, F. Zhao, and P. M. Kopittke, "Nanotechnology: A New Opportunity in Plant Sciences," *Trends in Plant Science* 21 (2016): 699–712.

69. A. Avellan, J. Yun, B. P. Morais, E. T. Clement, S. M. Rodrigues, and G. V. Lowry, "Critical Review: Role of Inorganic Nanoparticle Properties on Their Foliar Uptake and in Planta Translocation," *Environmental Science & Technology* 55 (2021): 13417–13431.

70. N. R. Burgos, P. J. Tranel, J. C. Streibig, et al., "Review: Confirmation of Resistance to Herbicides and Evaluation of Resistance Levels," *Weed Science* 61 (2013): 4–20.

71. D. Wang, N. B. Saleh, A. Byro, et al., "Nano-Enabled Pesticides for Sustainable Agriculture and Global Food Security," *Nature Nanotechnology* 17 (2022): 347–360.

72. Y. Xiao, C. Wu, P. Cui, X. Luo, L. Zhou, and Q. Yin, "Enhancing Adsorption Capacity and Herbicidal Efficacy of 2,4-D Through Supramolecular Self-Assembly: Insights From Cocrystal Engineering to Solution Chemistry," *Chemical Engineering Journal* 469 (2023): 143757.

73. Y. Zhang and G. G. Goss, "Nanotechnology in Agriculture: Comparison of the Toxicity Between Conventional and Nano-Based Agrochemicals on Non-Target Aquatic Species," *Journal of Hazardous Materials* 439 (2022): 129559.

74. X. Kong, B. Zhang, and J. Wang, "Multiple Roles of Mesoporous Silica in Safe Pesticide Application by Nanotechnology: A Review," *Journal of Agricultural and Food Chemistry* 69 (2021): 6735–6754.

75. P. L. Chariou, A. B. Dogan, A. G. Welsh, G. M. Saidel, H. Baskaran, and N. F. Steinmetz, "Soil Mobility of Synthetic and Virus-Based Model Nanopesticides," *Nature Nanotechnology* 14 (2019): 712–718.

76. M. D. S. Silva, D. S. Cocenza, R. Grillo, et al., "Paraquat-Loaded Alginate/Chitosan Nanoparticles: Preparation, Characterization and Soil Sorption Studies," *Journal of Hazardous Materials* 190 (2011): 366–374.

77. X. Wang, Y. Wang, X. Ma, M. Saleem, Y. Yang, and Q. Zhang, "Ecotoxicity of Herbicide Diuron on the Earthworm *Eisenia fetida*: Oxidative Stress, Histopathology, and DNA Damage," *International Journal of Environmental Science and Technology* 20 (2023): 6175–6184.

78. M. da Silva Simões, L. Bracht, A. V. Parizotto, J. F. Comar, R. M. Peralta, and A. Bracht, "The Metabolic Effects of Diuron in the Rat Liver," *Environmental Toxicology and Pharmacology* 54 (2017): 53–61.

79. Y. El-Nahhal and R. Lubbad, "Acute and Single Repeated Dose Effects of Low Concentrations of Chlorpyrifos, Diuron, and Their Combination on Chicken," *Environmental Science and Pollution Research* 25 (2018): 10837–10847.

80. D. Behrens, J. Rouxel, T. Burgeot, and F. Akcha, "Comparative Embryotoxicity and Genotoxicity of the Herbicide Diuron and Its Metabolites in Early Life Stages of *Crassostrea gigas*: Implication of Reactive Oxygen Species Production," *Aquatic Toxicology* 175 (2016): 249–259.

81. T. R. R. Lima, N. A. Kohori, J. L. V. de Camargo, C. A. da Silva, and L. C. Pereira, "Diuron and Its Metabolites Induce Mitochondrial Dysfunction-Mediated Cytotoxicity in Urothelial Cells," *Toxicology Mechanisms and Methods* 34 (2024): 32–45.

82. J. Je and S. Kim, "Reactive Oxygen Species Scavenging Activity of Aminoderivatized Chitosan With Different Degree of Deacetylation," *Bioorganic & Medicinal Chemistry* 14 (2006): 5989–5994.

83. J. Conceição, O. Adeoye, H. M. Cabral-Marques, et al., "Cyclodextrins as Excipients in Tablet Formulations," *Drug Discovery Today* 23 (2018): 1274–1284.

84. V. J. Stella and R. A. Rajewski, "Sulfobutylether-β-Cyclodextrin," *International Journal of Pharmaceutics* 583 (2020): 119396.

85. M. Anraku, J. M. Gebicki, D. Iohara, et al., "Antioxidant Activities of Chitosans and Its Derivatives in In Vitro and In Vivo Studies," *Carbohydrate Polymers* 199 (2018): 141–149.

86. Y. Peng, Y. Yu, Z. Su, et al., "Novel Ionic Chitosan Derivatives Based on Pyridinium Sulfonate: Synthesis, Characterization, and Studies on Antimicrobial, Antioxidant, and Biocompatibility Properties," *International Journal of Biological Macromolecules* 285 (2025): 138638.

87. X. Zhang, L. Hou, Z. Guo, et al., "Lipid Peroxidation in Osteoarthritis: Focusing on 4-Hydroxynonenal, Malondialdehyde, and Ferroptosis," *Cell Death Discovery* 9 (2023): 320.

Supporting Information

Additional supporting information can be found online in the Supporting Information section.

Supporting File 1: agt270299-sup-0001-SuppMat.docx.

Supporting File 2: agt270299-sup-0002-SuppMat.zip.